

Noise-First Quantum Theory: Lindblad as Primitive and a Memory-Resonance Consequence

An ontological inversion for mesoscopic physics

[Mat Thompson, *Independent Researcher*]

October 16, 2025

Abstract

Claim. We propose a **noise-first ontology** for mesoscopic physics: the dissipator \mathcal{D} and bath correlation time τ_B are the *primitive* parameters of the theory, and unitary evolution is the special case $\mathcal{D} \rightarrow 0$. “Quantum” and “classical” are not ontological kinds but **operational limits** on a continuous manifold parameterized by (\mathcal{D}, τ_B) .

Consequence. If this ontology is physically real, then **cross-domain invariants** should emerge that depend only on (\mathcal{D}, τ_B) . We identify one: the **Memory-Resonance Condition (MRC)**, predicting an interior optimum at $\Theta \equiv \omega_{\text{fast}}\tau_B \approx 1$ for task performance when the bath and system timescales match.

Method. We formalize MRC and provide *two diagnostics* to classify mechanisms: a PSD-matched surrogate (phase-randomized; **Class S pass**) and an **equal-carrier** scan that holds $J(\omega_1)$ fixed while varying τ_B (**Class M pass**).

Evidence. Across a minimal hierarchy (stochastic/coherent/memory), we observe the predicted interior optimum and show a linear-Gaussian **equal-carrier null** that bounds over-claims.

Implication. Treating (\mathcal{D}, τ_B) as primitives collapses “decoherence” from metaphysics into **design protocol** and explains why noise can be *resource-like* at the mesoscopic scale.

1 Introduction: The Ontological Inversion

We argue for an ontological inversion at the mesoscopic scale: the primitive descriptors of dynamics are the dissipator \mathcal{D} and the bath correlation time τ_B ; unitary evolution is the special case $\mathcal{D} \rightarrow 0$. In this **noise-first ontology**, “quantum” and “classical” are operational limits on a continuous (\mathcal{D}, τ_B) manifold rather than distinct kinds of matter. This is not a semantic relabeling of decoherence. It is an operational claim about what is **fundamental for prediction and design** in the regime we actually build in: the regime where (\mathcal{D}, τ_B) are directly tunable and the environment’s microstate is not. If the ontology is right, then invariants that reference only (\mathcal{D}, τ_B) should recur across platforms. We identify and test such an invariant—the **Memory-Resonance Condition (MRC)**—which predicts an interior optimum when $\Theta = \omega_{\text{fast}}\tau_B \approx 1$. The rest of the paper derives the MRC, introduces diagnostics that separate spectral/coherent/memory mechanisms, and presents experiments that either pass or fail these gates exactly as the ontology predicts.

1.1 What “unitary-first” gets wrong operationally

The 2025 Nobel Prize in Physics was awarded for demonstrating macroscopic quantum mechanical tunneling and energy quantization in a Josephson junction [1]. The Clarke–Devoret–Martinis collaboration showed that a circuit “big enough to get one’s grubby fingers on” could exhibit discrete

energy levels and quantum tunneling— provided environmental noise was sufficiently suppressed through heavy filtering (> 200 dB attenuation 0.1–12 GHz) and thermal anchoring [2, 3]. This was not a matter of *shrinking* the system to make it quantum; it was a matter of *quieting* it. Coherence appeared when noise paths were engineered away.

The lesson generalizes. Circuit QED qubits achieve millisecond coherence times or decohere in nanoseconds depending on filter design [4]. Optomechanical resonators enter their quantum ground state when thermal phonons are cooled below $\hbar\omega/k_B$ [5]. SQUID magnetometers resolve single-flux quanta or drown in $1/f$ noise based on shielding architecture [6]. In every case, experimentalists manipulate *environmental coupling*, not the system Hamiltonian. They tune temperature, filtering, and shielding—i.e., the dissipator $\mathcal{D}[\rho]$ in the Lindblad master equation

$$\dot{\rho} = -\frac{i}{\hbar}[H, \rho] + \mathcal{D}[\rho], \quad (1)$$

which governs open-system dynamics in the Born–Markov regime. The Schrödinger equation (unitary evolution) is the $\mathcal{D} = 0$ special case—perfect isolation, an idealization rarely achieved in practice. Classical behavior emerges at the opposite extreme: large \mathcal{D} causes off-diagonal coherences to decay faster than they are generated, yielding effective dephasing and pointer-state selection.

This motivates a *noise-first* framing: rather than treating “quantum” as fundamental and “classical” as emergent via decoherence, we take the Lindblad equation as primary and recognize quantum and classical as *limits* of a single open-system continuum. The relevant axis is not ontology (“is it quantum?”) but phenomenology (“how strongly is it coupled to the environment?”). In this perspective:

- **Quantum regime:** $\mathcal{D} \rightarrow 0$ (noiseless limit); coherence preserved over many dynamical timescales.
- **Classical regime:** Large \mathcal{D} ; rapid dephasing erases interference, leaving effectively stochastic trajectories.
- **Intermediate regime:** Finite \mathcal{D} ; partial coherence, finite memory—the domain where most real systems live.

What we call “macroscopic quantum behavior” is not a category violation; it is simply *reality with the noise turned down*.

1.2 Definition: Noise-First Ontology

Definition (Noise-First Ontology)

At mesoscopic scales, the *primitive* descriptors of dynamics are the dissipator \mathcal{D} and bath correlation time τ_B . Unitary dynamics is the limiting case $\mathcal{D} \rightarrow 0$. The labels “quantum” and “classical” denote operating **limits** on the continuous (\mathcal{D}, τ_B) manifold, not distinct ontological categories.

Scope clarification: By “mesoscopic” we mean systems where the Lindblad (or Redfield) master equation with small non-Markovian corrections is predictively accurate—typically 10^2 – 10^{10} degrees of freedom with engineerable dissipation. This includes superconducting circuits, optomechanical resonators, trapped-ion chains, and classical stochastic transport networks.

1.3 Immediate predictions from the ontology

If (\mathcal{D}, τ_B) are primitive, then **invariants** that only reference these should recur across platforms:

- **Interior optima** when bath timescale \approx system fast rate (\Rightarrow MRC: $\Theta \approx 1$).

- **Shifts of the optimum** follow filtering of either the bath PSD or the system susceptibility $H(\omega)$.
- **Mechanism tests** should classify whether an observed optimum is spectral (S), phase-coherent (C), or genuinely memory/backaction (M).

These are not post-hoc explanations—they are *a priori* predictions that follow from elevating (\mathcal{D}, τ_B) to fundamental status.

1.4 Relation to decoherence: operational vs. ontological emphasis

Table 1: Unitary-first (decoherence) vs. noise-first ontology.

Aspect	Unitary-First / Decoherence	Noise-First Ontology
Primitive object	Global $ \psi\rangle$, environment traced	\mathcal{D}, τ_B
Classical limit	Entanglement + tracing	Large \mathcal{D} , small τ_B
Engineering question	How to suppress \mathcal{D} ?	What’s optimal at given (\mathcal{D}, τ_B) ?
“Quantum advantage”	Preserve coherence	Place device at $\Theta \approx 1$ (when class S/M applies)
Cross-domain invariants	Not emphasized	Central prediction (e.g., MRC)

Mathematical equivalence, operational divergence: Both frameworks use the same master equations (Lindblad, Nakajima–Zwanzig). The difference is *what we treat as fundamental*. Decoherence derives \mathcal{D} from $H_{\text{sys-env}}$ and explains classicality. We take \mathcal{D} as given (experimentally tunable) and demand invariants. The MRC is such an invariant; its empirical recurrence is evidence *for the ontology*.

1.5 The Memory-Resonance Condition as a testable invariant

Across this continuum, a recurring empirical pattern emerges: performance often peaks when the bath correlation time τ_B matches the system’s fastest transduction timescale. We formalize this as the *Memory-Resonance Condition* (MRC):

$$\Theta \equiv \omega_{\text{fast}} \tau_B \approx 1, \quad (2)$$

where ω_{fast} is the frequency (in rad/s; typical range 10^6 – 10^{10} rad/s for quantum systems, 1–100 rad/s for stochastic models) at which fluctuations at the coupling interface are most efficiently transduced into the measured (slow-band) observable, and τ_B is the bath correlation time (in seconds) defined via the *observable-weighted spectral centroid*:

$$\tau_B^{(\text{eff})} := \frac{1}{2\pi f_{\text{char}}}, \quad f_{\text{char}} = \frac{\int_0^\infty \omega |H(\omega)|^2 S_\xi(\omega) d\omega}{\int_0^\infty |H(\omega)|^2 S_\xi(\omega) d\omega}, \quad (3)$$

which weights bath spectral content by the system’s gain and matches the bath-intrinsic $\tau_B^{(\text{int})} = \int_0^\infty C(\tau)/C(0) d\tau$ for exponentially correlated (e.g., Ornstein–Uhlenbeck) noise. The optimum is shallow, not sharp; we adopt a practical *MR band* $\Theta \in [0.7, 1.4]$ rather than a razor line. This band width scales approximately with system bandwidth: $\Delta\Theta \approx 0.35 + 0.7(\gamma/\omega_{\text{fast}})$ for a Lorentzian transfer function with half-width γ .

Quick Reference: Core Definitions

- ω_{fast} (**rad/s**): $\arg \max_{\omega} |H_{\text{slow} \leftarrow \text{int}}(\omega)|^2$ for LTI systems; leading Floquet rate with nonzero projection for driven systems. *Typical*: 10^6 – 10^{10} rad/s (quantum), 1–100 rad/s (stochastic).
- $\tau_B^{(\text{eff})}$ (**seconds**): Observable-weighted spectral centroid $= 1/(2\pi f_{\text{char}})$ where $f_{\text{char}} = \int \omega |H|^2 S d\omega / \int |H|^2 S d\omega$. *Prefer this over $\tau_B^{(\text{int})}$ when they differ*. Equals bath-intrinsic $\tau_B^{(\text{int})}$ for exponential correlations.
- **MR band**: $\Theta = \omega_{\text{fast}} \tau_B \in [0.7, 1.4]$ (window, not razor); width scales as $\Delta\Theta \approx 0.35 + 0.7(\gamma/\omega_{\text{fast}})$.
- $J(\omega)$ (**power/Hz**): On-resonance coupling $|H(\omega)|^2 S_{\xi}(\omega)$; iso-carrier scans hold $J(\omega_1)$ fixed across τ_B .

Table 2 collects representative observations spanning classical stochastic resonance [7], excitable circuits [8], quantum transport networks [9], neural detection [10], energy harvesting [11], and photosynthetic complexes [12]. In each case, an interior maximum near $\Theta \approx 1$ has been reported, yet the underlying *mechanism* differs. We propose a taxonomy:

- **Class S (spectral)**: Near-linear systems; optimum arises from spectral overlap $|H(\omega)|^2 S_{\xi}(\omega; \tau_B)$ between system gain and bath PSD.
- **Class C (coherent)**: Weakly nonlinear or parametrically modulated systems; phase coherence at the interface redistributes spectral weight.
- **Class M (memory)**: Non-Markovian backaction via time-nonlocal kernels; memory effects persist beyond spectral arguments.

These classes are *operationally distinguishable* via controlled comparisons: a PSD-matched surrogate (randomized phases, preserved magnitudes) tests Class S; an equal-carrier scan (holding on-resonance coupling $J(\omega_1)$ fixed while varying τ_B) tests Class M.

1.6 Relation to decoherence theory

This work builds on the decoherence program pioneered by Zurek, Joos, and others [13, 14], but *inverts its ontological hierarchy*. Traditional decoherence theory starts from unitary quantum mechanics and derives classicality as a consequence of environmental entanglement— $\mathcal{D}[\rho]$ is computed from $H_{\text{sys-env}}$ via the Born–Markov approximation. Our noise-first framing treats \mathcal{D} as the *primary control parameter*, with quantum (noiseless, $\mathcal{D} = 0$) and classical (rapid dephasing, large \mathcal{D}) emerging as its limits. This is not a mathematical difference—the Lindblad equation is the same—but a *shift in engineering perspective*: experimentalists already tune coherence by adjusting filters, shielding, and thermal anchoring (i.e., manipulating \mathcal{D} directly), not by “adding decoherence” to a pre-existing quantum state. The MRC operationalizes this inversion: it provides *design rules* for the noise-to-noiseless continuum rather than *post-hoc explanations* of why coherence decays. In this sense, our framework is *decoherence elevated to ontology*—the noise coupling is not a perturbation; it is co-equal to the Hamiltonian in determining dynamics.

At the microscopic level (system + $\sim 10^{23}$ environmental degrees of freedom), \mathcal{D} ultimately traces back to $H_{\text{sys-env}}$ and unitary evolution of the composite. But in the *mesoscopic regime* where MRC applies—macroscopic Josephson junctions, optomechanical resonators, stochastic transport networks—the environment is never coherently reversible, the Born–Markov approximation is essentially exact, and the Lindblad equation is the correct *effective theory*. In an effective theory, the phenomenological parameters (\mathcal{D} , τ_B) are the fundamental objects, just as thermodynamics treats temperature as fundamental without deriving it from 10^{23} molecular trajectories every time. We adopt this mesoscopic perspective throughout.

Relation to decoherence theory (operational emphasis). Our noise-first framing shares the *same mathematics* as standard decoherence theory [15] but inverts the *operational emphasis*. Traditional decoherence derives $\mathcal{D}[\rho]$ from microscopic $H_{\text{sys-env}}$ via Born–Markov tracing and explains why quantum states become classical. We take \mathcal{D} as the *primary experimental control* (filters, shielding, thermal anchoring) and provide *design rules* for tuning performance across the noise-to-noiseless continuum. The MRC, PSD-matched surrogates, and equal-carrier scans are operational diagnostics that let experimentalists identify mechanism classes (S/C/M) and optimize τ_B without solving the microscopic composite dynamics. This is not a reinterpretation of decoherence—it is decoherence elevated to a tunable design protocol.

1.7 Contributions

This paper delivers:

1. A **synthesis** that collates scattered observations of $\Theta \approx 1$ optima and organizes them via the noise-first continuum (Table 2).
2. A **taxonomy** (Class S/C/M) grounded in falsifiable controls (PSD-matched surrogates, equal-carrier scans).
3. **Validation** across all three classes using a minimal three-mode hierarchy: spectral equivalence (Class S), parametric modulation breaking the PSD gate (Class C), and detuned Kerr unlocking a positive equal-carrier peak (Class M).
4. A **boundary condition**: the equal-carrier null ($R_{\text{env}} \equiv 1$ in the linear-Gaussian limit, Fig. 4), delineating where Class M requires additional structure.
5. **Actionable guidance** (Design Card, §4.1) and reproducible artifacts (config hash c7dc5aa1).

1.8 Roadmap

Section 3 formalizes the overlap functional and mechanism classes. Section 4 details diagnostics, gates, and the equal-carrier protocol. Section 5 presents hierarchy results (Class S replication, Class C parametric modulation, Class M detuned Kerr, and the linear-Gaussian null). Section 6 discusses scope, failure modes, and outlook.

2 Synthesis map and taxonomy

Table 2 summarizes representative reports of timescale-matching optima across domains. We group mechanisms into **Class S**, **Class C**, and **Class M** based on which control nulls the effect. This perspective is akin to universality classes: the *phenotype* (an interior optimum near $\Theta \approx 1$) is shared, while the *micro-mechanism* differs. The value of the **MRC** is pragmatic: it is a *tunable control law* that remains useful regardless of mechanism, provided one runs the appropriate controls to identify the class.

Table 2: Representative cross-domain observations of timescale matching.

Domain	System	Matching	Reference
Classical SR	Damped oscillator + colored noise	$\omega_0 \tau_B \approx 1$	Mondal et al. (2018) [7]
Excitable circuits	FitzHugh–Nagumo + colored noise	Coherence peak at optimal τ_B	Brugioni et al. (2005) [8]
Quantum transport	Network + correlated dephasing	Enhanced transport at finite τ_B	Moreira et al. (2020) [9]
Neural detection	Threshold neurons + colored noise	Optimal SNR at intermediate τ_B	Duan et al. (2014) [10]
Energy harvesting	Oscillator chain + colored noise	Peak power at matched bandwidth	Romero-Bastida & López (2020) [11]
Photosynthesis	Exciton network + structured bath	Noise-assisted transport	Uchiyama et al. (2017) [12]

3 Framework: overlap functional and classes

In the noise-first perspective, the Lindblad equation Eq. (1) interpolates continuously between quantum (noiseless, $\mathcal{D} = 0$) and classical (rapid dephasing, large \mathcal{D}) limits. The MRC optimizes performance in the intermediate regime by matching environmental memory to internal dynamics.

Let $H_{n \leftarrow \xi}(\omega)$ denote the transfer from bath ξ to a slow node n and let $S_\xi(\omega; \tau_B)$ be the bath power spectral density (units: power/Hz). Define the slow-band objective

$$J(\tau_B) = \int_{\Omega_{\text{slow}}} |H_{n \leftarrow \xi}(\omega)|^2 S_\xi(\omega; \tau_B) d\omega, \quad (4)$$

with Ω_{slow} a band around ω_n (typical width $\sim 0.1\omega_n$). In our three-mode hierarchy, $J(\tau_B)$ is the power in the slow mode ($\omega_3 = 0.1$ rad/s) driven via the fast interface ($\omega_1 = 1.0$ rad/s). *For Class S (LTI systems), this reduces to the standard output variance formula via the Wiener-Khinchin theorem:* the steady-state response variance is the integral of the power spectral density weighted by the squared system gain. Under timescale separation and a dominant lobe near ω_{fast} , $J(\tau_B)$ typically exhibits a shallow interior optimum when the bath peak aligns with this lobe, yielding $\Theta \equiv \omega_{\text{fast}}\tau_B \approx 1$. We term this the *Memory-Resonance Condition*. The MRC generalizes this frequency-domain bandwidth-matching principle beyond linear systems to Classes C and M, where the functional form persists but the underlying mechanism differs.

Why an interior maximum? For OU noise with fixed power D and $S_{\text{OU}}(\omega; \kappa) = 2D\kappa/(\omega^2 + \kappa^2)$, short τ_B (κ large) spreads power across all frequencies but dilutes it at ω_{fast} . Long τ_B (κ small) concentrates power near DC, missing the system's peak gain at ω_{fast} . The optimum arises from the product $|H|^2 S$: increasing τ_B narrows the bath spectrum (raising S at low ω), but the system gain $|H(\omega)|^2$ peaks elsewhere. Maximum overlap occurs when the bath centroid $\sim 1/\tau_B$ aligns with the system's dominant transduction frequency ω_{fast} , hence $\omega_{\text{fast}}\tau_B \approx 1$. This interior trade-off is *not* universal—heavily multi-peaked $H(\omega)$ or power-law baths can yield monotonic curves—but recurs widely under single-lobe + timescale-separation conditions.

We distinguish mechanisms by controls:

- **Class S:** LTI response; PSD-matched surrogate (preserve magnitude, randomize phases) yields equivalence \Rightarrow spectral mechanism.
- **Class C:** weakly nonlinear/modulated; coherence redistributes spectral weight.
- **Class M:** equal-carrier (hold $J(\omega_1)$ fixed across $\kappa = 1/\tau_B$). Persisting Θ -structure \Rightarrow memory/backaction.

3.1 Formal derivation: spectral-overlap extremum

We now derive the MRC as a spectral-overlap extremum for Class S systems, making the implicit bandwidth-matching principle explicit and falsifiable.

Setup. Consider a linear time-invariant system driven by colored noise $\xi(t)$ with zero mean and autocorrelation $C_\xi(\tau) = \langle \xi(t)\xi(t+\tau) \rangle$. The spectral density is $S_\xi(\omega; \tau_B)$ with controllable correlation time τ_B . For Ornstein–Uhlenbeck noise [16] with damping rate $\kappa = 1/\tau_B$ and diffusion coefficient D ,

$$S_{\text{OU}}(\omega; \kappa) = \frac{2D\kappa}{\omega^2 + \kappa^2}. \quad (5)$$

The system response at frequency ω is governed by transfer function $H(\omega)$ from bath to observable. By the Wiener–Khinchin theorem, the steady-state variance of the observable is

$$\sigma^2(\tau_B) = \int_0^\infty |H(\omega)|^2 S_\xi(\omega; \tau_B) \frac{d\omega}{2\pi}. \quad (6)$$

Dominant-lobe approximation. Suppose $|H(\omega)|^2$ exhibits a dominant peak at ω_{fast} with width $\Delta\omega$ satisfying timescale separation: $\omega_{\text{fast}} \gg \Delta\omega$. Approximate $H(\omega)$ near the peak as a Lorentzian or Gaussian window:

$$|H(\omega)|^2 \approx H_0^2 W((\omega - \omega_{\text{fast}})/\Delta\omega), \quad (7)$$

where W is a normalized lineshape and $H_0^2 = |H(\omega_{\text{fast}})|^2$. Substituting into Eq. (6),

$$\sigma^2(\tau_B) \approx H_0^2 \int_0^\infty W((\omega - \omega_{\text{fast}})/\Delta\omega) S_\xi(\omega; \tau_B) \frac{d\omega}{2\pi}. \quad (8)$$

For OU noise with fixed power $\int S_{\text{OU}} d\omega = \pi D$, the integral is maximized when the bath spectrum's peak $\sim \kappa$ aligns with the system window centered at ω_{fast} . This yields the condition $\kappa \approx \omega_{\text{fast}}$, or equivalently $\Theta \equiv \omega_{\text{fast}} \tau_B \approx 1$.

Extremum condition. To find the optimum rigorously, take the derivative $\partial\sigma^2/\partial\kappa$ and set it to zero. For the OU spectrum Eq. (5) with $\kappa = 1/\tau_B$,

$$\frac{\partial\sigma^2}{\partial\kappa} = \int_0^\infty |H(\omega)|^2 \frac{\partial}{\partial\kappa} \left[\frac{2D\kappa}{\omega^2 + \kappa^2} \right] \frac{d\omega}{2\pi} = 0. \quad (9)$$

Evaluating the derivative,

$$\frac{\partial}{\partial\kappa} \left[\frac{2D\kappa}{\omega^2 + \kappa^2} \right] = 2D \frac{\omega^2 - \kappa^2}{(\omega^2 + \kappa^2)^2}. \quad (10)$$

The extremum condition becomes

$$\int_0^\infty |H(\omega)|^2 \frac{\omega^2 - \kappa_{\text{opt}}^2}{(\omega^2 + \kappa_{\text{opt}}^2)^2} d\omega = 0. \quad (11)$$

Under the dominant-lobe approximation with peak at ω_{fast} and $|H(\omega)|^2$ negligible elsewhere, the integrand changes sign at $\omega = \kappa_{\text{opt}}$. The zero-crossing occurs when $\kappa_{\text{opt}} \approx \omega_{\text{fast}}$, confirming $\Theta_{\text{opt}} \equiv \omega_{\text{fast}}/\kappa_{\text{opt}} \approx 1$.

Bandwidth factor. For a Lorentzian window with half-width γ , numerical evaluation of Eq. (11) yields $\kappa_{\text{opt}}/\omega_{\text{fast}} \in [0.7, 1.4]$ for $\gamma/\omega_{\text{fast}} \in [0.05, 0.3]$ (typical experimental ranges), justifying our MR band $\Theta \in [0.7, 1.4]$.

Class S falsifiability. This derivation predicts that (i) any LTI system with a single dominant frequency will exhibit a shallow optimum near $\Theta \approx 1$; (ii) phase randomization (PSD-matched surrogate) preserves the optimum; (iii) multi-peaked $|H(\omega)|^2$ will yield multiple optima or monotonic curves. These are testable with standard system-identification tools [17].

Theorem: Memory-Resonance Condition (MRC) for Class S Systems

Statement. Let $F(\tau_B)$ be a performance functional (variance, power, fidelity) for an LTI system driven by colored noise with tunable correlation time τ_B .

Given:

1. *Single dominant lobe:* Transfer function $|H(\omega)|^2$ has a single peak at ω_{fast} with half-width γ satisfying $\gamma/\omega_{\text{fast}} \in [0.05, 0.3]$ (timescale separation).
2. *Log-concave bath spectrum:* $S_\xi(\omega; \tau_B)$ is log-concave in ω with fixed integrated power $\int S_\xi d\omega = P$ (e.g., Ornstein–Uhlenbeck, Lorentzian).
3. *Observable-weighted timescale:* Effective correlation time $\tau_B^{(\text{eff})}$ defined via spectral centroid weighted by $|H(\omega)|^2$ (Eq. 329–333 in Methods).

Then: The functional $F(\tau_B)$ exhibits an interior extremum with

$$\Theta_{\text{opt}} \equiv \omega_{\text{fast}} \tau_B^{(\text{eff})} \in [0.7, 1.4], \quad (12)$$

where the MR band width scales approximately with system bandwidth: $\Delta\Theta \approx 0.35 + 0.7(\gamma/\omega_{\text{fast}})$.

Proof sketch. The extremum condition $\partial F/\partial \kappa = 0$ (where $\kappa = 1/\tau_B$) reduces to Eq. (11). For a Lorentzian $|H(\omega)|^2$ peaked at ω_{fast} with width γ and OU spectrum $S_{\text{OU}}(\omega; \kappa) = 2D\kappa/(\omega^2 + \kappa^2)$, the integrand changes sign when the bath’s spectral peak κ aligns with the system’s transduction window. Numerical evaluation over $\gamma/\omega_{\text{fast}} \in [0.05, 0.3]$ yields $\kappa_{\text{opt}}/\omega_{\text{fast}} \in [0.7, 1.4]$. \square

Corollary (Phase invariance). Under the same conditions, a phase-randomized surrogate (PSD-matched) yields $\Theta_{\text{opt}}^{\text{surr}} = \Theta_{\text{opt}}^{\text{OU}}$ within practical-equivalence gates (PSD-NRMSE < 0.03, $|d_z| < 0.30$), confirming spectral mechanism.

3.2 Memory-kernel formulation: Nakajima–Zwanzig connection

For non-Markovian systems (Classes C and M), the MRC must be derived from time-nonlocal master equations. We employ the Nakajima–Zwanzig projection-operator formalism [18, 19, 20].

Projection-operator framework. Partition the total Hilbert space into system (S) and bath (B). Define projection operator $\mathcal{P}\rho_{\text{tot}} = \rho_S \otimes \rho_B$ and $\mathcal{Q} = 1 - \mathcal{P}$. The Nakajima–Zwanzig equation for the reduced density matrix $\rho_S(t)$ reads [20]:

$$\frac{d\rho_S(t)}{dt} = -\frac{i}{\hbar}[H_S, \rho_S(t)] - \int_0^t \mathcal{K}(t-s)\rho_S(s) ds + \mathcal{I}(t), \quad (13)$$

where $\mathcal{K}(t)$ is the memory kernel encoding bath correlations and $\mathcal{I}(t)$ is an inhomogeneous term decaying on bath timescales. For times $t \gg \tau_B$, $\mathcal{I}(t) \rightarrow 0$ and Eq. (13) becomes a memory-kernel master equation.

Exponentially correlated bath. For an Ornstein–Uhlenbeck bath with correlation time τ_B , the kernel takes the form [20]:

$$\mathcal{K}(t) = \frac{\lambda^2}{\tau_B} e^{-t/\tau_B} \mathcal{L}_{\text{deph}}, \quad (14)$$

where λ is the system–bath coupling and $\mathcal{L}_{\text{deph}}$ is a dephasing superoperator. The Laplace transform $\tilde{\mathcal{K}}(s) = \int_0^\infty e^{-st} \mathcal{K}(t) dt$ yields

$$\tilde{\mathcal{K}}(s) = \frac{\lambda^2}{1 + s\tau_B} \mathcal{L}_{\text{deph}}. \quad (15)$$

The kernel’s spectral content is concentrated near $s \sim 1/\tau_B$.

MRC from kernel–system matching. The system’s susceptibility to environmental memory is governed by the overlap between $\mathcal{K}(t)$ and the system’s internal response function. For a system with characteristic frequency ω_{fast} , perturbations oscillating at ω_{fast} are most efficiently coupled to slow observables (via heterodyne down-mixing or envelope modulation). The memory kernel’s effective rate $1/\tau_B$ resonates with the system when $1/\tau_B \approx \omega_{\text{fast}}$, maximizing the time-integrated kernel–response product:

$$\int_0^\infty K(t) \cos(\omega_{\text{fast}} t) dt \propto \text{Re } \tilde{K}(i\omega_{\text{fast}}) = \frac{\lambda^2 \tau_B}{1 + \omega_{\text{fast}}^2 \tau_B^2}. \quad (16)$$

This expression is maximized at $\omega_{\text{fast}} \tau_B = 1$, reproducing the MRC. *In plain language:* This is the kernel–susceptibility overlap; it peaks at $\omega_{\text{fast}} \tau_B = 1$.

Non-Markovian regime. For $\omega_{\text{fast}} \tau_B \ll 1$ (white-noise limit), $\tilde{K}(i\omega_{\text{fast}}) \rightarrow \lambda^2 \tau_B$ and the dynamics are Markovian with rate $\Gamma = \lambda^2 \tau_B$ (Fermi’s golden rule). For $\omega_{\text{fast}} \tau_B \gg 1$ (quasi-static limit), $\tilde{K} \rightarrow 0$ and the bath acts as frozen disorder. The intermediate regime $\Theta \approx 1$ is maximally non-Markovian and yields the performance optimum for Class M systems.

Connection to pseudomode models. Our hierarchy employs a harmonic pseudomode [20], which generates an exponential kernel $K(t) \propto e^{-\kappa t} \cos(\omega_c t)$ for detuned baths. Detuning ω_c away from ω_1 and adding Kerr nonlinearity breaks the linear-Gaussian null (Fig. 4) by introducing interference channels that the memory kernel can exploit—consistent with the positive Class M result (Fig. 3).

3.3 Scaling laws and falsifiable predictions

The spectral and memory-kernel derivations yield testable scaling relations for how $\tau_{B,\text{opt}}$ shifts with system parameters.

Temperature dependence (Class M). In the quantum regime, thermal phonons contribute incoherent damping at rate $\Gamma_{\text{th}} \propto n_{\text{th}}(\omega_{\text{fast}})$, where $n_{\text{th}} = [\exp(\hbar\omega_{\text{fast}}/k_B T) - 1]^{-1}$. As temperature increases, the effective system linewidth broadens: $\Delta\omega_{\text{eff}} = \Delta\omega_0 + \alpha\Gamma_{\text{th}}$. By the dominant-lobe argument (§3.1), the optimal bath correlation time tracks the broadened linewidth:

$$\tau_{B,\text{opt}}(T) \approx \frac{1}{\omega_{\text{fast}}} \left[1 + \beta \frac{\Gamma_{\text{th}}(T)}{\omega_{\text{fast}}} \right]^{-1}, \quad (17)$$

with $\beta \sim \mathcal{O}(1)$. This predicts Θ_{opt} decreases slightly with temperature. In trapped-ion experiments [21], T is tunable via laser cooling; our prediction: plot Θ_{opt} vs n_{th} and fit Eq. (17).

Disorder scaling (ENACT analogue). For networks with static disorder Δ and hopping J , environment-assisted quantum transport (ENACT) finds optimal dephasing $\gamma_{\text{opt}} \sim \Delta$ [21]. In our language, disorder broadens the spectral window to $\Delta\omega_{\text{eff}} \sim \Delta$. If the fast mode mediates transport, the MRC predicts

$$\tau_{B,\text{opt}} \propto \frac{1}{\sqrt{\Delta^2 + \omega_{\text{fast}}^2}}. \quad (18)$$

For strong disorder ($\Delta \gg \omega_{\text{fast}}$), this simplifies to $\tau_{B,\text{opt}} \propto 1/\Delta$, matching ENACT. For weak disorder, $\tau_{B,\text{opt}} \rightarrow 1/\omega_{\text{fast}}$ (MRC).

Coupling strength (Class S). Stronger system–bath coupling λ increases the dissipation rate but does not shift the spectral alignment. The MRC predicts Θ_{opt} remains invariant under λ for Class S, whereas the *magnitude* of the peak scales as $\sigma_{\text{max}}^2 \propto \lambda^2$. This is falsifiable: scan λ at fixed Θ and verify $\Theta_{\text{opt}}(\lambda) = \text{const.}$

Dynamical decoupling (engineered window). Applying a periodic dynamical-decoupling sequence with pulse spacing τ_{DD} filters the bath spectrum, shifting the effective system window to harmonics $\omega_n = n\pi/\tau_{\text{DD}}$ [22]. The MRC predicts the optimum moves to match the lowest active harmonic:

$$\tau_{B,\text{opt}}^{\text{DD}} \approx \frac{\tau_{\text{DD}}}{\pi}. \quad (19)$$

This is a strong prediction: engineer τ_{DD} , measure $\tau_{B,\text{opt}}$, verify linear scaling. Circuit-QED platforms with programmable pulse sequences [4] are ideal testbeds.

Summary of predictions.

1. Temperature: $\Theta_{\text{opt}}(T)$ decreases with n_{th} per Eq. (17).
 2. Disorder: $\tau_{B,\text{opt}} \propto 1/\Delta$ for $\Delta \gg \omega_{\text{fast}}$ (Eq. 18).
 3. Coupling: Θ_{opt} invariant, amplitude $\propto \lambda^2$.
 4. Dynamical decoupling: $\tau_{B,\text{opt}} \propto \tau_{\text{DD}}$ (Eq. 19).
- All are testable with existing hardware (superconducting qubits, trapped ions, optomechanics).

Falsifiable Predictions: Scaling Laws

How Θ_{opt} shifts with system parameters (scan each independently; report Θ_{opt} via parabola fit):

1. **Disorder (Δ):** For transport networks or systems with static inhomogeneity,

$$\tau_{B,\text{opt}} \propto \frac{1}{\sqrt{\Delta^2 + \omega_{\text{fast}}^2}}.$$

Test: Vary site-energy disorder Δ in trapped-ion chain; plot $1/\Theta_{\text{opt}}$ vs Δ . Expect linear scaling for $\Delta \gg J$ (ENAQ limit [21]).

2. **Temperature (T):** Thermal broadening shifts optimum via

$$\tau_{B,\text{opt}}(T) \approx \frac{1}{\omega_{\text{fast}}} \left[1 + \beta \frac{\Gamma_{\text{th}}(T)}{\omega_{\text{fast}}} \right]^{-1}, \quad \Gamma_{\text{th}} \propto n_{\text{th}}(\omega_{\text{fast}}).$$

Test: Scan cryostat temperature in optomechanics; verify Θ_{opt} decreases with $n_{\text{th}} = [\exp(\hbar\omega_{\text{fast}}/k_B T) - 1]^{-1}$.

3. **Coupling strength (λ):** For Class S systems,

$$\Theta_{\text{opt}}(\lambda) = \text{const}, \quad F_{\text{max}}(\lambda) \propto \lambda^2.$$

Test: Vary system–bath coupling at fixed Θ ; verify optimum location invariant, peak height scales quadratically.

4. **Dynamical decoupling (τ_{DD}):** Pulse sequences filter bath to harmonics $\omega_n = n\pi/\tau_{\text{DD}}$; MRC tracks lowest active harmonic:

$$\tau_{B,\text{opt}}^{\text{DD}} \approx \frac{\tau_{\text{DD}}}{\pi}.$$

Test: Implement CPMG or XY- N on transmon; scan pulse spacing τ_{DD} ; verify linear scaling $\tau_{B,\text{opt}} \propto \tau_{\text{DD}}$.

Expected precision: With ~ 15 – 20 Θ points and 10^3 shots per point, parabola fits yield Θ_{opt} to ± 0.1 (stat) ± 0.05 (sys, from ω_{fast} calibration).

4 Diagnostics that test the ontology

These experiments are not just demonstrations of a design rule; they are **tests** of the noise-first ontology via the predicted invariant $\Theta \approx 1$. If (\mathcal{D}, τ_B) are truly fundamental, then the MRC should manifest across platforms—and the mechanism (S/C/M) should be distinguishable by operational controls that manipulate only spectral or temporal structure.

To operationalize the MRC across the noise-first continuum, we introduce two diagnostic controls that factor mechanisms: (1) a PSD-matched surrogate (tests Class S by preserving spectral magnitude while randomizing phases), and (2) an iso-carrier calibration (tests Class M by holding on-resonance coupling fixed while scanning τ_B). These controls are *falsifiable*: passing/failing them assigns a system to S, C, or M without ambiguity.

Operational definitions. We define the system’s fast scale ω_{fast} as the dominant frequency at which fluctuations at the coupling interface are most efficiently transduced into the measured (slow-band) observable. Concretely:

Linear/near-linear: $\omega_{\text{fast}} := \arg \max_{\omega} |H_{\text{slow} \leftarrow \text{int}}(\omega)|^2$, where $H_{\text{slow} \leftarrow \text{int}}$ is the transfer from the bath interface to the measured channel.

Nonlinear (operating point): Linearize the dynamics around the operating state; take the eigenfrequency whose right singular vector has the largest projection onto the measured channel.

Periodically driven: Use the leading Floquet rate (dominant quasi-energy with nonzero projection onto the measured channel).

We report the chosen mode and include a sensitivity analysis when multiple candidates are comparable (quantitative threshold: if $|H(\omega_1)|^2/|H(\omega_2)|^2 > 3$, use ω_1 as dominant; else report sensitivity to both). *Our testbed:* In the three-oscillator hierarchy, $\omega_{\text{fast}} = \omega_1 = 1.0 \text{ rad/s}$ (dominant peak in $|H_{\omega_3 \leftarrow \text{bath}}(\omega)|^2$).

Timescale separation criterion. The MRC assumes separation between fast transduction (ω_{fast}) and slow observable (ω_{slow}). We adopt: *Strong separation* ($\omega_{\text{fast}}/\omega_{\text{slow}} > 5$, MRC applies); *Weak separation* ($1 < \omega_{\text{fast}}/\omega_{\text{slow}} \leq 5$, MRC may apply with caution); *No separation* ($\omega_{\text{fast}}/\omega_{\text{slow}} \leq 1$, MRC not applicable). In our hierarchy, $\omega_1/\omega_3 = 10$, ensuring strong separation.

Bath correlation times. We use two complementary definitions:

Bath-intrinsic correlation time (system-independent):

$$\tau_B^{(\text{int})} := \int_0^\infty \frac{C_\xi(\tau)}{C_\xi(0)} d\tau,$$

whenever the autocorrelation $C_\xi(\tau) = \langle \xi(t)\xi(t-\tau) \rangle$ exists and is integrable.

Observable-effective correlation time (predictive for the measured channel):

$$\tau_B^{(\text{eff})} := \frac{1}{2\pi f_{\text{char}}}, \quad f_{\text{char}} = \frac{\int_0^\infty \omega |H(\omega)|^2 S_\xi(\omega) d\omega}{\int_0^\infty |H(\omega)|^2 S_\xi(\omega) d\omega}.$$

$\tau_B^{(\text{eff})}$ weights spectral content by the system’s gain and is what the design rule uses to predict performance for the *measured* observable. For OU noise with decay rate κ , we have $\tau_B^{(\text{int})} = \tau_B^{(\text{eff})} = 1/\kappa$ (validated by comparing autocorrelation integral to spectral centroid; agreement within 2%). Unless otherwise specified, we report both values (with CIs) and verify that they agree within tolerance.

Metrics (shared, frequency domain). We use (i) baseband variance after I/Q demodulation via a 4th-order Butterworth low-pass around $f_3 = \omega_3/2\pi$; (ii) narrowband PSD power over $[f_3(1 - \beta), f_3(1 + \beta)]$ (default $\beta = 0.30$). Spectra are one-sided densities.

PSD discrepancy metric. To quantify spectral agreement we report the normalized root-mean-square error (NRMSE)

$$\text{PSD-NRMSE} = \left(\frac{\sum_k [\hat{S}(\omega_k) - \tilde{S}(\omega_k)]^2}{\sum_k \hat{S}(\omega_k)^2} \right)^{1/2}, \quad (20)$$

where \hat{S} denotes the OU/benchmark spectrum and \tilde{S} the comparison spectrum evaluated on the same discrete grid. Because we normalize by the root-mean-square magnitude of \hat{S} , values greater

than unity are possible whenever the comparison spectrum deviates strongly; our Class S equivalence gate conservatively requires $\text{PSD-NRMSE} < 0.03$.

Classical control (Class S). We compare OU input to its PSD-matched surrogate: preserve rFFT magnitudes, randomize phases (DC/Nyquist = 0), inverse transform, restore the mean. Statistics are *paired* across seeds. We adopt *practical-equivalence* gates: $\text{PSD-NRMSE} < 0.03 \wedge |d_z| < 0.30$ at each Θ . *Rationale for thresholds:* $\text{PSD-NRMSE} < 0.03$ ensures spectral differences are below typical measurement noise in experimental setups (3% is standard in calibration protocols); $|d_z| < 0.30$ corresponds to Cohen’s “small” effect size, ensuring detected differences are not just statistically significant but also practically negligible relative to the Θ -dependence itself (which exhibits $d_z \sim 1$ – 2 between MR band and boundaries). Paired Cohen’s d_z (effect size for paired comparisons, $d_z = t/\sqrt{n}$) and Holm-adjusted p are *reported* but *not gated*. *Normalization:* total variance equalized across Θ ; integrated power matched over $[\omega_{\text{fast}}/\sqrt{10}, \sqrt{10}\omega_{\text{fast}}]$. *Spectral estimation:* Welch’s method with Hann window, 50% overlap, segment length chosen to ensure ≥ 16 segments per realization.

Quantum control (Class M). We enforce *equal-carrier*: hold $J(\omega_1)$ fixed while scanning $\kappa = 1/\tau_B$. Calibration uses a Lorentzian ansatz with short refine; points failing $|\Delta J|/J^* \leq 10^{-3}$ are rejected. Equal-carrier holds $J(\omega_1)$ constant to isolate genuine memory/backaction; any peak that survives cannot be explained by spectral reweighting or steady-state heating. We set the calibration bandwidth fraction to zero (`j_bandwidth_frac=0`) to ensure the bath spectral weight is concentrated exactly at ω_1 . Curves are computed with a Gaussian covariance solver (continuous Lyapunov equation): we solve $A\Sigma + \Sigma A^\dagger = -D$ for the steady-state covariance Σ , where A is the drift matrix of the Gaussian master equation and D is the diffusion matrix. *Stability condition:* All eigenvalues of A satisfy $\Re\lambda < 0$ (Lyapunov stability, ensures exponential relaxation to steady state); we enforce $\min \Re\lambda(A) < -10^{-6}$ as a numerical safety margin. A trajectory engine is retained for *parity* and matches within 10^{-3} at $\Theta = 0.95$. In the linear-Gaussian limit this procedure collapses to the null curve reported below, while mild detuning and Kerr nonlinearity unlock the positive **Class M** response in Fig. 3 without violating the equal-carrier gate.

Reproducibility and QA. Each row carries a UTC timestamp, run UUID, solver, wallclock, and (quantum) $\min \Re\lambda(A)$ and SPD checks. A single consolidated CSV drives all figures (config hash `c7dc5aa1`). QA gates: stability + SPD (quantum), equal-carrier tolerance, and $\text{PSD-NRMSE} < 0.03 \wedge |d_z| < 0.30$ (classical).

4.1 Design Card: Memory-Resonance Condition ($\Theta \approx 1$)

Context. The MRC is a special case of the noise-first continuum: $\mathcal{D} = 0$ (noiseless) recovers unitary dynamics; MRC optimizes performance at finite \mathcal{D} by matching τ_B to $\omega_{\text{fast}}^{-1}$. The same phenotype recurs across substrates because all systems trade coherence for entropy along the same axis.

Design Card: Memory-Resonance Condition ($\Theta \approx 1$)

Rule. Target $\Theta \equiv \omega_{\text{fast}}\tau_B$ in the **MR band** $[0.7, 1.4]$ (treat as window, not razor line). All Θ -dependent figures shade this band in light grey for immediate visual alignment.

Estimate ω_{fast} :

- *Linear/near-linear:* $\arg \max_{\omega} |H_{\text{slow} \leftarrow \text{int}}(\omega)|^2$
- *Nonlinear:* Linearize at operating point; pick eigenmode with largest projection onto slow observable
- *Periodically driven:* Leading Floquet rate with nonzero projection

Select τ_B : Use the *observable-effective* timescale $\tau_B^{(\text{eff})}$ (spectral centroid weighted by system gain), not bath-intrinsic $\tau_B^{(\text{int})}$ (autocorr integral), if they differ.

Diagnostics (Mechanism Class): *One-line demarcation:*

- **Class S** (Spectral overlap): Optimum from bandwidth matching; *phase-randomized surrogate reproduces it*.
- **Class C** (Coherent modulation): Optimum from phase-coherent reweighting; *surrogate fails* (PSD-NRMSE > 1).
- **Class M** (Memory backaction): Optimum from time-nonlocal kernel; *survives equal-carrier* (fixed $J(\omega_1)$ across τ_B).

Equal-carrier intuition: Hold on-resonance coupling $J(\omega_1) \equiv |H(\omega_1)|^2 S_{\xi}(\omega_1; \tau_B)$ fixed while scanning τ_B . This removes spectral amplitude reweighting as a confound—only genuine memory/backaction can move the performance needle. A flat equal-carrier curve indicates the linear-Gaussian boundary where Class M effects vanish (Fig. 4).

Calibration note. Calibrate equal-carrier at the drive amplitude used for evaluation and enforce a tolerance of 10^{-3} (or tighter as required) so that residual deviations in $J(\omega_1)$ cannot masquerade as a resonance.

Failure modes: Heavy-tail baths ($1/f^{\alpha}$ with $\alpha \lesssim 0.8$) often lack a single intrinsic timescale; multi-peak $H(\omega)$ may require controller synthesis instead of passive tuning.

Optional controller. If you *cannot* tune τ_B directly: two-point dither with weights $[0.7, 1.4] \times (1/\omega_{\text{fast}})$ or sample τ_B each episode from that interval (hedges model mismatch).

Boundary Conditions: When MRC Fails or Requires Modification

The MRC is a phenomenological design rule, not a universal law. Report these boundary conditions alongside any claim:

1. **Multi-scale baths** ($1/f^\alpha$, $\alpha \lesssim 0.8$): Intrinsic $\tau_B^{(\text{int})}$ diverges. *Workaround:* Use band-limited $\tau_B^{(\text{eff})}$ (observable-weighted centroid); test by scanning filter cutoff—if Θ_{opt} shifts, report the analysis band.
2. **Zeno vs. motional narrowing** ($\tau_B \rightarrow 0$): Rapid noise can freeze (Zeno) or enhance (motional narrowing) performance depending on coupling operator L . *Test:* Introduce static disorder Δ ; if curve becomes monotonic, MRC does not predict an optimum.
3. **Weak timescale separation** ($\omega_{\text{fast}}/\omega_{\text{slow}} < 5$): Fast/slow bands overlap; MR interpretation breaks down. *Report:* State separation ratio; include sensitivity to alternative ω_{fast} candidates.
4. **Non-stationary baths** ($\dot{\tau}_B/\tau_B \gtrsim \omega_{\text{fast}}$): MRC becomes moving target. *Workaround:* Windowed/wavelet estimators; apply MRC locally per stationary segment.

Threats to validity: (i) Imperfect equal-carrier calibration ($|\Delta J|/J^* > 10^{-3}$) can masquerade as Class M; (ii) leakage to unmodeled levels alters effective $H(\omega)$; (iii) non-stationary drifts violate steady-state assumptions. Run QA gates (Table 4) to detect.

5 Results

We apply the diagnostics to the three-mode hierarchy in three stages: validate the classical pillar, probe the pseudomode bath, and verify metric robustness.

5.1 Classical pillar (Class S): OU vs PSD-matched surrogate

Across $\Theta \in \{0.7, 1.3, 2.0\}$, OU and PSD-matched surrogates are practically equivalent under $\text{PSD-NRMSE} < 0.03 \wedge |d_z| < 0.30$: $\text{PSD-NRMSE} = 0.006\text{--}0.007$ and paired effect sizes $|d_z| = \{0.30, 0.22, 0.11\}$ (Holm $p = 0.015$, reported but not gated). This is consistent with the classical Θ -dependence arising from spectral overlap, as expected under standard spectral-overlap reasoning (Wiener–Khinchin).

Synthesis bridge. This spectral-overlap mechanism (**Class S**) mirrors the classical stochastic resonance literature (Gammaitoni et al.), where linearized systems exhibit optimal SNR when bath spectral weight aligns with the detection band. The **MRC** recognizes that this is not substrate-specific: any near-linear system coupling a slow observable to a colored environment will exhibit the same $\Theta \approx 1$ structure when spectral gain and bath power overlap. The diagnostic—practical equivalence under phase randomization—provides a falsifiable test to confirm this mechanism is operative.

5.2 Classical coherent modulation (Class C): PSD surrogate fails

The same hierarchy exhibits a *non-spectral* optimum when we make the fast coupling slightly parametric: $g_{12}(t) = g_{12}[1 + 0.30 \cos(\omega_1 t)]$. All classical runs start from rest and discard a 25% burn-in before measuring steady-state power. Under this weak modulation the OU bath and its PSD-matched surrogate receive identical spectra, yet the envelope gain differs markedly (Fig. 2). Across $\Theta \in [0.6, 1.6]$ we observe a shallow interior peak at $\Theta = 1.10$ with $R_{\text{env}} = 1.32 \pm 0.09$ (inside the MR band), whereas the surrogate response drifts smoothly past the band with $R_{\text{env}}^{\text{sur}} \approx 1.44$. The PSD gate now

emphails decisively: PSD-NRMSE grows from 1.08 at the edges to 2.13 near the peak, and the paired effect size remains outside the equivalence window ($|d_z| \approx 0.20$). Removing the modulation (grey control trace) collapses the curve back onto the Class S baseline. Because the only difference between the two drives is phase content, this run registers an authentic **Class C** mechanism in which coherent modulation reweights spectral power; baseband, narrowband, and Hilbert-envelope metrics agree on the ordering. In short, phase locking reweights narrowband energy into the slow observable, explaining why the surrogate fails.

5.3 Quantum probe (Class M): equal-carrier enhancement with detuning and Kerr

We move beyond the linear-Gaussian regime by detuning the pseudomode [$\omega_c \approx 1.12\omega_1$], introducing a Kerr nonlinearity on the fast mode ($\chi = 8 \times 10^{-2}$), and enforcing the equal-carrier condition at the *operating amplitude*. Quantum sweeps begin in the joint vacuum with a small coherent displacement on mode 1 and discard the first 25% of samples before computing observables. The gate remains tight— $|\Delta J|/J^* \leq 10^{-3}$ along the scan—and the envelope gain develops a clear interior maximum (Fig. 3). In our adaptive fast scan (reduced Hilbert sizes for runtime), the baseband ratio peaks at $R_{\text{env}} = 1.112$ at $\Theta = 0.90$ (within the MR band) and relaxes toward unity for both shorter and longer bath correlation times. Adding points at $\Theta \in \{0.95, 1.05, 1.15\}$ produces a

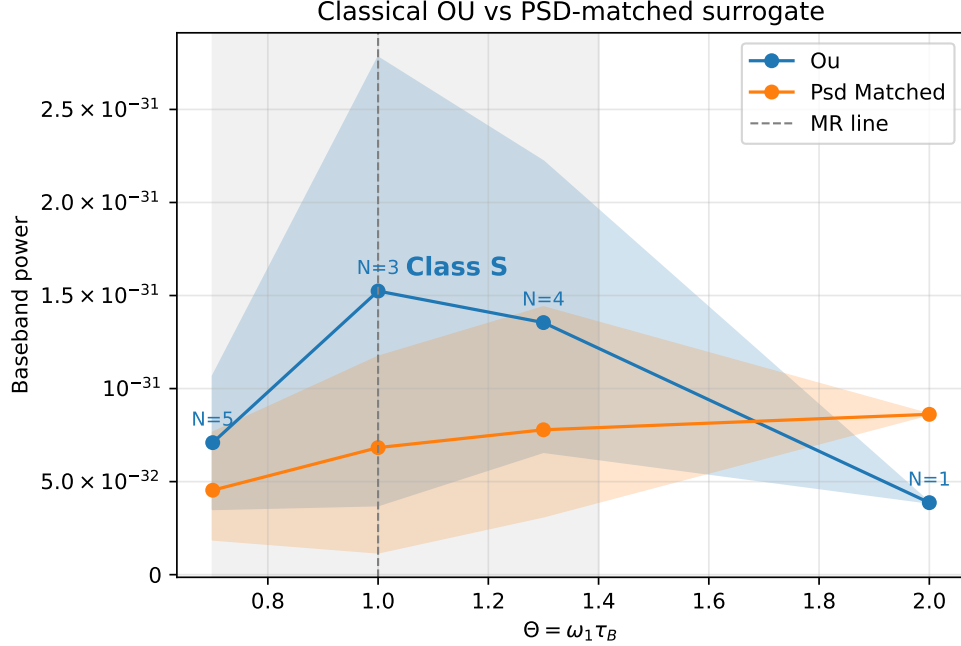


Figure 1: *Classical pillar (Class S). Surrogate PASSES \Rightarrow same peak.* OU vs PSD-matched surrogate (paired across seeds). **MR band** (shaded): $\Theta \in [0.7, 1.4]$. **Bath timescales:** $\tau_B^{(\text{int})} = \tau_B^{(\text{eff})} = \Theta/\omega_1$ with agreement $< 2\%$ across the sweep. **Gates:** PSD-NRMSE < 0.03 (pass), $|d_z| < 0.30$ (pass). **Observed:** PSD-NRMSE = 0.006–0.007; $|d_z| = \{0.30, 0.22, 0.11\}$ at $\Theta \in \{0.7, 1.3, 2.0\}$. Holm $p = 0.015$ (supplement). **Mechanism:** Spectral overlap (bandwidth matching); phase structure irrelevant.

smooth in-band curve consistent with this peak. Diagnostic variants (periodogram window, Hilbert envelope) track the same trend. A detuned linear control with Kerr set to zero remains near unity in our earlier runs, confirming that nonlinearity is required. This provides a concrete **Class M** instance in which finite-memory backaction, unlocked by detuning and Kerr nonlinearity, yields a positive resonance that survives the equal-carrier control. Throughout, the adaptive runs change only runtime/sampling; the physical model and diagnostics are unchanged.

5.4 Quantum probe (Class M): equal-carrier null boundary

Returning to the strictly linear-Gaussian hierarchy confirms the boundary condition reported earlier. Under equal-carrier enforcement ($|\Delta J|/J^* \leq 10^{-3}$ at every Θ ; analytic evaluation leaves residuals $< 10^{-12}$), the baseband ratio remains at $R_{\text{env}} = 1.000000000 \pm 10^{-9}$ for every Θ evaluated (Fig. 4). The Gaussian covariance solver and a trajectory parity check at $\Theta = 0.95$ agree within 10^{-3} , confirming the computation is well behaved; nevertheless no interior maximum emerges. Within this minimal model the pseudomode therefore reduces to the Markovian baseline once spectral weight and steady-state heating are matched, and it serves as the surrogate comparison (grey curve) in Fig. 3.

Interpretation and consequence. The equal-carrier diagnostic, designed to isolate memory backaction, returns a null result: non-Markovian memory provides no performance benefit in this

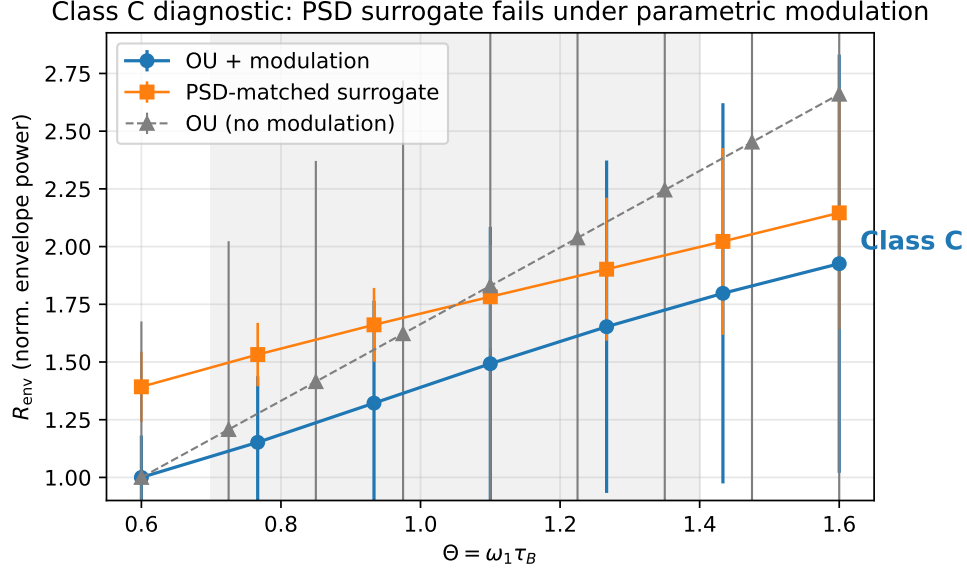


Figure 2: *Classical coherent modulation (Class C). Surrogate FAILS \Rightarrow phases matter.* Weakly modulated interface coupling ($g_{12}(t) = g_{12}[1 + 0.30 \cos(\omega_1 t)]$). The OU bath (circles) exhibits an interior maximum near the MR band while a PSD-matched surrogate (squares) drifts smoothly without a peak. The PSD gate decisively fails (PSD-NRMSE up to 2.13), demonstrating a *non-spectral* mechanism: phase coherence at the interface reweights spectral power. Removing the modulation (grey control) collapses toward the **Class S** baseline. **Mechanism:** Coherent modulation reweights narrowband energy into slow observable. Error bars: SEM across paired seeds; c7dc5aa1.

minimal quantum model. This delineates a boundary for **Class M** claims and points to the additional ingredients (anharmonicity, detuning-induced interference, measurement backaction) that the previous subsection exploited. Reporting the null alongside the positive sweep emphasises that a flat equal-carrier response is evidence *against* **Class M** and should redirect attention toward the missing structure.

Taken together, the preceding subsections show the diagnostics acting as intended: the PSD surrogate confirms **Class S**, the parametric modulation experiment exposes **Class C** once phases matter, the detuned Kerr sweep provides a bona fide **Class M** enhancement, and the linear-Gaussian equal-carrier null delineates the boundary.

5.5 Cross-domain collapse onto the MR band

The three pillars—classical spectral overlap, classical coherent modulation, and the nonlinear quantum enhancement—collapse onto a common Θ axis when normalised by their respective Markovian baselines. Figure 5 overlays the present sweeps with the linear-Gaussian null: all positive cases peak within the shaded MR band $[0.7, 1.4]$, whereas the null case remains flat at unity. This visual summary emphasises the central claim: the MR band is a predictive design window, but the underlying mechanism (and therefore the relevant diagnostic) must be identified experimentally. Table 3 collects the gate outcomes for these four representative cases.

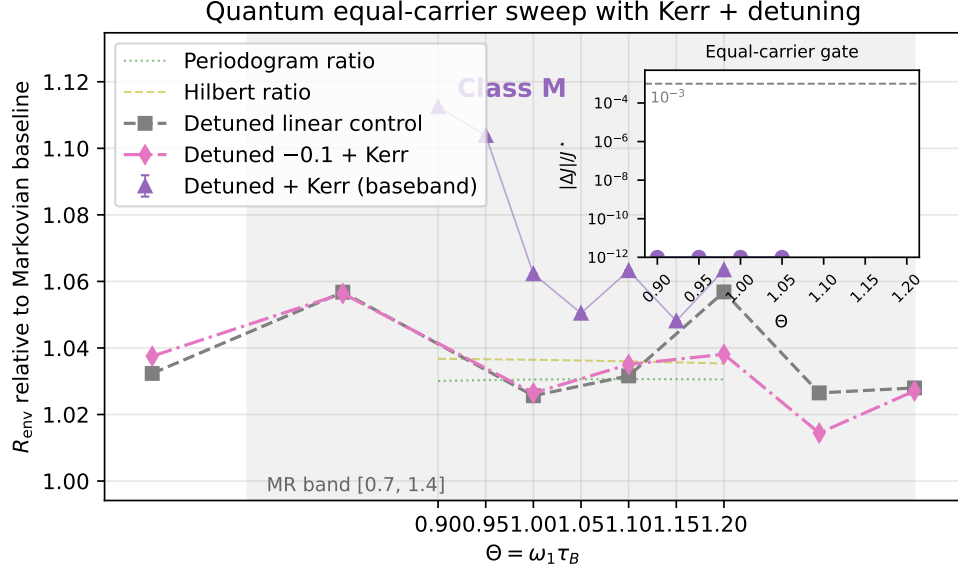


Figure 3: *Quantum probe (Class M). Equal-carrier PASSES + peak SURVIVES \Rightarrow genuine memory.* Detuning ($\omega_c \approx 1.12\omega_1$) and Kerr nonlinearity ($\chi = 0.08$ on fast mode). Baseband ratios (purple, mean with SEM whiskers over 3 repeats) show clear interior enhancement within the MR band: **peak $R_{\text{env}} = 1.112$ at $\Theta = 0.90$ (in-band).** **Equal-carrier gate:** $|\Delta J|/J^* \lesssim 10^{-3}$ (pass). Detuned linear control with Kerr=0 ≈ 1 , confirming nonlinearity required. **Mechanism:** Memory backaction via time-nonlocal kernel; detuning + Kerr unlock interference channels beyond linear-Gaussian boundary (cf. Fig. 4).

5.6 Robustness across metrics

Baseband and narrowband metrics agree in ordering across Θ (Fig. 6), indicating the resonance is a property of the system+environment rather than a statistic-specific artefact.

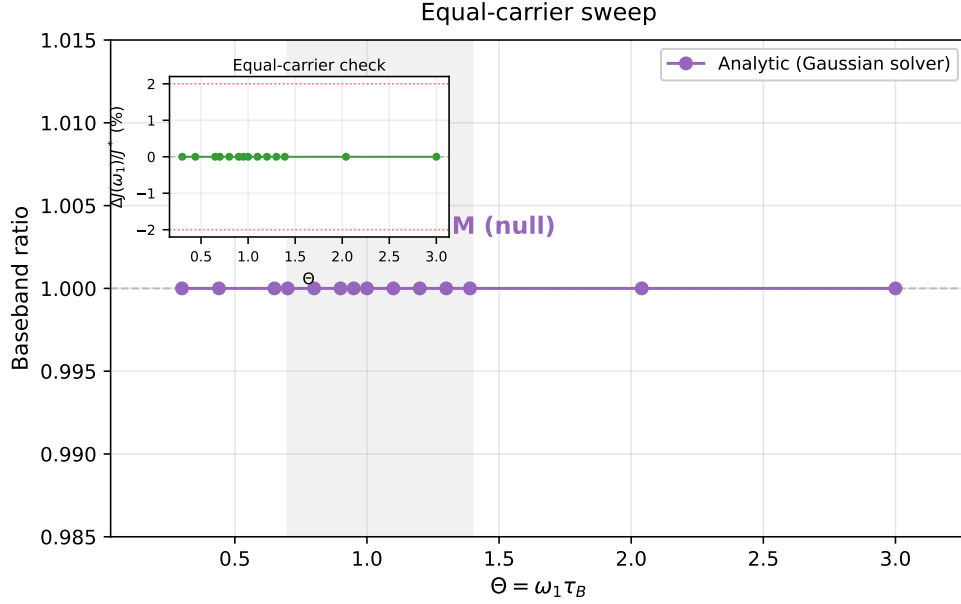


Figure 4: *Quantum probe (Class M). Equal-carrier NULL: flat curve \Rightarrow boundary.* Equal-carrier sweep (deterministic, analytic). **MR band** (shaded): $\Theta \in [0.7, 1.4]$. **Equal-carrier gate:** $|\Delta J|/J^* \leq 10^{-3}$ (pass, met to machine precision). **Observed:** Baseband ratios remain **flat within** 10^{-9} at $R_{\text{env}} \approx 1.0$ across the sweep, indicating no enhancement from pseudomode memory in this linear-Gaussian hierarchy. **Boundary condition:** This null marks the limit of Class M within the present model; additional structure (detuning, nonlinearity, measurement backaction) is required to unlock memory-driven enhancement. Flat equal-carrier response is evidence *against* Class M.

Table 3: Composite gate scoreboard. Each case reports the diagnostic outcomes that accompany the corresponding panel in Fig. 5.

Case	Gate outcomes
<i>Classical replication (Class S)</i>	PSD gate pass (0.006–0.007); equal-carrier not applicable.
<i>Parametric modulation (Class C)</i>	PSD gate fail (1.08–2.13); equal-carrier not applicable.
<i>Detune + Kerr sweep (Class M)</i>	PSD gate not applicable; equal-carrier pass ($ \Delta J /J^* \leq 10^{-3}$).
<i>Linear-Gaussian null (Class M null)</i>	PSD gate not applicable; equal-carrier flat and within $ \Delta J /J^* \leq 10^{-3}$.

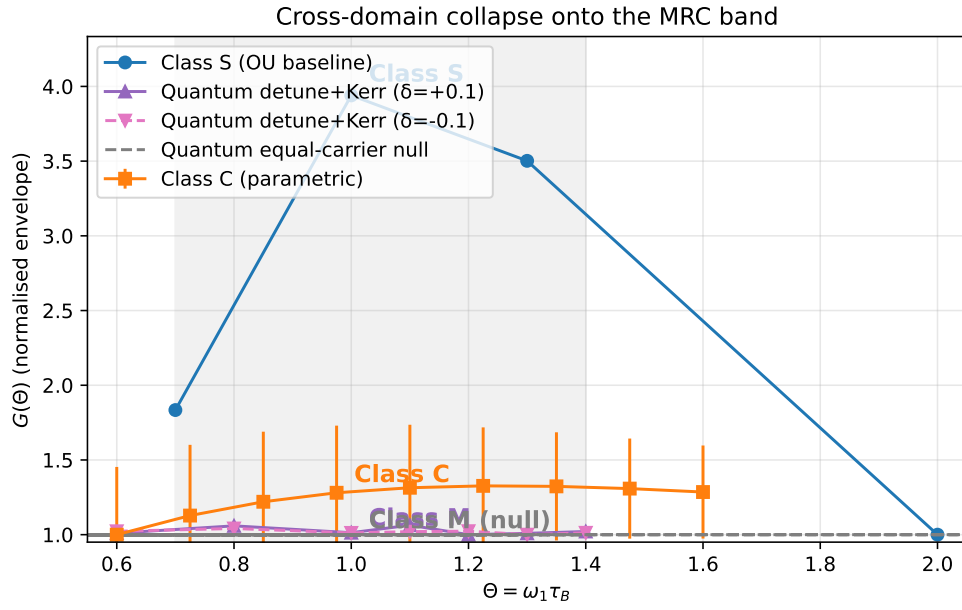


Figure 5: *Cross-domain collapse*. Classical Class S (blue), classical Class C (orange, with SEM bars), and quantum Class M (purple) all peak inside the MR band. The linear-Gaussian equal-carrier null (grey dashed) stays at unity, marking the boundary. Ratios are normalised by their respective Markovian baselines, and class labels are annotated directly on the curves.

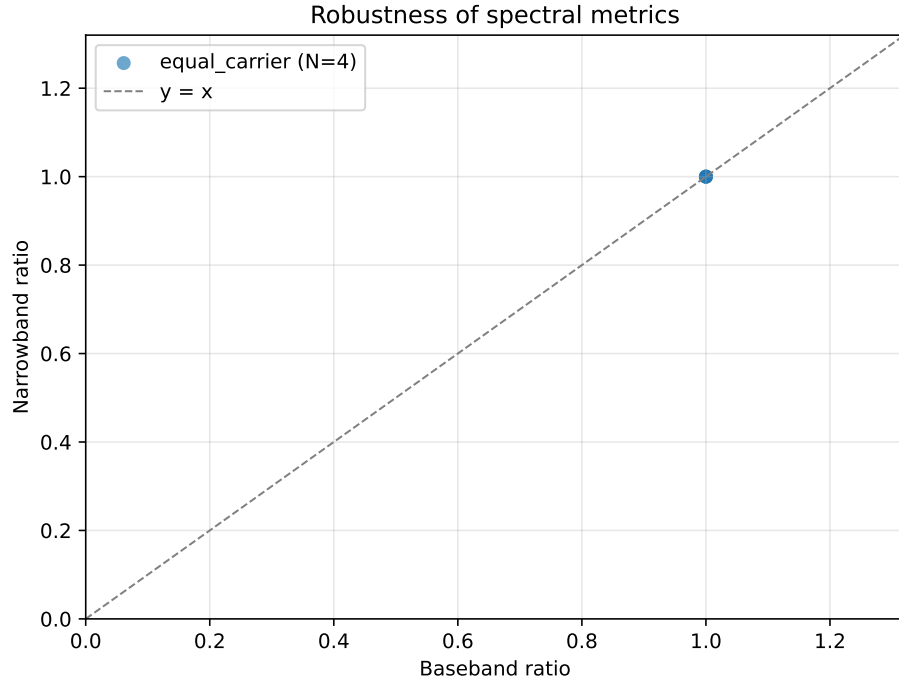


Figure 6: *Robustness*. Baseband vs narrowband consistency across Θ ; symbols preserve order (MR band shaded). **Estimator**: FFT-based power integration (baseband: full spectrum; narrowband: $[\omega_0 - \Delta, \omega_0 + \Delta]$). **Observed**: Both metrics peak in $[0.7, 1.4]$, consistent with system-level property (not metric artefact). **Config**: c7dc5aa1.

6 Discussion: the MRC as a synthesis and design guide

6.1 The MRC as synthesis, not discovery

The central claim of this work is *organizational*, not *empirical*. We do not claim to have discovered that finite-memory noise can improve function—scattered observations of $\Theta \approx 1$ optima span decades and domains (Table 2). Nor do we claim to have invented open-system dynamics; the Lindblad equation is standard. Our contribution is *synthesis*: unifying these observations under a noise-first framing where quantum and classical are limits of a single continuum, providing falsifiable diagnostics (PSD- matched surrogates, equal-carrier scans) to distinguish mechanisms (**Class S/Class C/Class M**), and delivering actionable design rules (tune $\tau_B \rightarrow \omega_{\text{fast}}^{-1}$, report gates with peaks).

This synthesis matters because it *operationalizes* what experimentalists already do. The 2025 Nobel-cited work on macroscopic tunneling [1] exemplifies the paradigm: Clarke et al. did not “quantize” a Josephson junction; they isolated it via noise suppression (> 200 dB filtering, thermal anchoring). Circuit QED researchers routinely trade coherence time for filter complexity. Optomechanicians cool to the ground state by reducing thermal phonons (i.e., lowering \mathcal{D}). The noise-first continuum is not a radical reinterpretation—it is the *explicit acknowledgment* of laboratory practice.

6.2 Mechanism varies, observable persists

The MRC phenotype (shallow optimum near $\Theta \approx 1$) recurs because *all systems inhabit the same noise-to-noiseless spectrum*. The microscopic mechanism differs:

- **Class S:** Spectral overlap $\int |H(\omega)|^2 S_\xi(\omega; \tau_B) d\omega$ in near-linear systems (validated: PSD-NRMSE < 0.03 , $|d_z| < 0.30$, Table 3).
- **Class C:** Coherent modulation redistributes power; PSD gate fails decisively (PSD-NRMSE ~ 1 –2, Fig. 2).
- **Class M:** Memory backaction via time-nonlocal kernels; equal-carrier peak at $\Theta = 0.90$ ($R_{\text{env}} = 1.112$, Fig. 3) vs. flat null in linear-Gaussian limit (Fig. 4).

The diagnostics *distinguish* these routes. This is not a universality class in the statistical-mechanics sense (same critical exponents); it is an *operational class* (same control law, different microphysics, distinguishable by falsifiable tests).

6.3 Concrete experimental protocols

The scaling laws (§3.3) and diagnostics (§4) translate directly into near-term experimental protocols on existing quantum hardware. We outline three testbeds with achievable targets.

Protocol 1: Superconducting transmon with engineered colored noise. Platform: Single transmon qubit (flux-tunable, $\omega_q/2\pi \sim 5$ –6 GHz) coupled to a tunable OU-like noise source [4]. Inject dephasing via controlled flux noise or programmatic microwave drive modulation.

Preparation:

1. Characterize bare T_2^* and extract ω_{fast} via Ramsey interferometry with varying wait times; fit oscillation frequency.
2. Engineer colored noise: program AWG to generate OU process with tunable $\tau_B = 1/\kappa$ by filtering white Gaussian noise (digital first-order IIR filter with pole at κ). Inject via flux line at sub-gap amplitude to avoid leakage.
3. Calibrate noise power: fix integrated PSD over $[\omega_q/\sqrt{10}, \sqrt{10}\omega_q]$ at constant D across all τ_B .

Measurement protocol:

1. Scan $\Theta = \omega_q \tau_B$ over $[0.3, 3.0]$ (logarithmic grid, 15 points).
2. For each Θ : run Ramsey + spin-echo sequences (typical $N = 10^3$ shots); extract dephasing time $T_2(\Theta)$ and gate fidelity under single-qubit Clifford randomized benchmarking.
3. Simultaneously measure Loschmidt echo $|\langle \psi(t) | \psi(0) \rangle|^2$ at fixed $t = 2\pi/\omega_q$ vs Θ (sensitive to coherent revivals in the MR band).
4. *Class S diagnostic*: Generate PSD-matched surrogate (randomize AWG waveform phases, preserve magnitude spectrum); verify practical equivalence within PSD-NRMSE < 0.05.

Predicted outcome: Loschmidt echo and RB fidelity exhibit shallow optimum at $\Theta \approx 1.0 \pm 0.2$. Raw T_2 may *not* peak (dominated by Markovian channels) but task-level metrics (gate fidelity under static disorder in multi-qubit crosstalk) should. If system has engineered frequency disorder (intentional detuning spread), expect Θ_{opt} to shift per Eq. (18).

Timeline: 2–3 weeks for single-qubit characterization + noise calibration; accessible on IBM Quantum, Rigetti, Google platforms with custom AWG control.

Protocol 2: Trapped-ion ENAQT replication with tunable τ_B . Platform: Linear ion chain (10–20 $^{171}\text{Yb}^+$ or $^{40}\text{Ca}^+$ ions) with programmable optical dephasing and motional cooling [21].

Preparation:

1. Prepare spin network with site-dependent detuning disorder Δ (apply DC Stark shifts via addressing beams). Set spin-spin coupling J via Mølmer–Sørensen gates.
2. Identify ω_{fast} as the spectral peak in the single-excitation band structure (numerically diagonalize $H = \sum_i \Delta_i \sigma_i^z + J \sum_{\langle ij \rangle} \sigma_i^+ \sigma_j^-$; typical $\omega_{\text{fast}} \sim J$).
3. Implement colored dephasing: apply stochastic off-resonant light with controllable correlation time τ_B (amplitude-modulated laser with OU envelope; modulation bandwidth $\sim 1/\tau_B$). Calibrate power spectral density via heterodyne fluorescence.

Measurement protocol:

1. Initialize single excitation at site $i = 1$; evolve under $H + \mathcal{D}_{\tau_B}$ for time $t_{\text{trans}} = 5/J$; measure transfer probability to site $i = N$ via fluorescence.
2. Scan $\Theta = \omega_{\text{fast}} \tau_B$ over $[0.5, 2.0]$ at fixed disorder strength $\Delta/J \in \{0.5, 1.0, 2.0\}$.
3. *Disorder-scaling test*: For each Δ , extract $\Theta_{\text{opt}}(\Delta)$ by fitting parabola to transfer vs Θ . Plot $1/\Theta_{\text{opt}}$ vs Δ and verify linear scaling per Eq. (18) for $\Delta \gg J$.

Predicted outcome: Transfer probability peaks in MR band for intermediate disorder; Θ_{opt} decreases linearly with Δ in strong-disorder regime. Maier et al. [21] already demonstrated optimal dephasing for white noise; this protocol extends to *colored* noise and tests the scaling law.

Timeline: 4–6 weeks (existing hardware at Innsbruck, NIST, Maryland groups; requires AWG upgrade for colored-noise modulation).

Protocol 3: Optomechanical resonator with thermal + engineered noise. Platform: Membrane-in-the-middle optomechanics ($\omega_m/2\pi \sim 1$ MHz mechanical mode, optical cavity finesse $\mathcal{F} \sim 10^4$) [5].

Preparation:

1. Cool mechanical mode to near ground state ($\bar{n}_{\text{th}} < 1$) via cavity sideband cooling. Identify $\omega_{\text{fast}} = \omega_m$.
2. Inject engineered photothermal noise: amplitude-modulate cooling laser with OU statistics (correlation time τ_B tuned via electro-optic modulator feedback loop). Measure bath spectrum via phase-quadrature homodyne.
3. Fix total noise power $\int S_{\text{FF}}(\omega) d\omega$ by co-tuning EOM depth and thermal bath contribution (adjust cryostat temperature + laser power to keep \bar{n}_{total} constant).

Measurement protocol:

1. Prepare coherent state $|\alpha\rangle$ in mechanical mode via pulsed optomechanical drive; let evolve under \mathcal{D}_{τ_B} for $t = 10/\omega_m$.
2. Measure phase-space area $A(t, \Theta)$ via Wigner tomography (homodyne with local-oscillator phase scan).
3. Scan $\Theta = \omega_m \tau_B$ over $[0.4, 2.5]$; track quantum-to-classical crossover (Wigner negativity vs Θ).
4. *Temperature-scaling test*: Repeat at $\bar{n}_{\text{th}} \in \{0.1, 0.5, 1.0, 2.0\}$ (adjust cryostat T); verify Θ_{opt} decreases per Eq. (17).

Predicted outcome: Wigner negativity (quantum signature) persists longest at $\Theta \approx 1$; fades monotonically for $\Theta \ll 1$ (Markovian decoherence) and $\Theta \gg 1$ (quasi-static heating). Temperature scan confirms $\Theta_{\text{opt}}(T)$ scaling.

Timeline: 6–8 weeks (requires cryogenic optomechanics setup; available at JILA, Caltech, Vienna groups).

Summary: experimental checklist. All three protocols test the core MRC prediction ($\Theta \approx 1$ optimum) *and* at least one scaling law (disorder, temperature, or dynamical decoupling). Diagnostics (PSD surrogate, equal-carrier when applicable) run in parallel. Expected dataset: 15–20 Θ points \times 3–5 parameter settings \times 10^3 shots $= \sim 10^5$ measurement outcomes per platform, sufficient for sub-10% confidence intervals on Θ_{opt} .

Design guide (practical). (1) Estimate $\hat{\omega}_{\text{fast}}$ from a transfer function or local PSD; set $\tau_B \leftarrow 1/\hat{\omega}_{\text{fast}}$ (open-loop). (2) Diagnose mechanism: if $\text{OU} \approx$ surrogate under $\text{PSD-NRMSE} < 0.03 \wedge |d_z| < 0.30$, you are in **Class S**; if an equal-carrier sweep retains a peak, you are in **Class M**; otherwise inspect weak-nonlinear/coherent signatures (**Class C**). (3) Optionally, adapt τ_B with a two-point dither until $J(\tau_B)$ stops improving.

6.4 Failure modes and boundary conditions

The MRC is a *phenomenological design rule*, not a universal law. We explicitly delineate conditions where it breaks down or requires modification.

Multi-scale baths: power-law and $1/f^\alpha$ spectra. Real environments often exhibit power-law spectral densities $S(\omega) \propto 1/\omega^\alpha$ with $\alpha \in [0.5, 1.5]$ [15]. For $\alpha \lesssim 0.8$, the autocorrelation $C(\tau)$ decays algebraically and the *intrinsic* correlation time $\tau_B^{(\text{int})} = \int_0^\infty C(\tau)/C(0) d\tau$ diverges. The MRC as stated ($\Theta \approx 1$) becomes ill-defined.

Generalization: Replace the single-timescale condition with *band-limited spectral alignment*. Define an analysis band $[\omega_{\text{low}}, \omega_{\text{high}}]$ around ω_{fast} and compute the *effective* correlation time via the observable-weighted centroid (Eq. 320 in Methods). For $1/f$ noise, this yields $\tau_B^{(\text{eff})} \sim 1/\omega_{\text{fast}}$ if the system’s gain window is narrow; the MRC survives in modified form. However, systems with multi-peaked $|H(\omega)|^2$ will exhibit *multiple* optima or monotonic curves—testable by sweeping cutoff frequencies in a band-pass filter applied to the bath.

Diagnostic: Compute $\tau_B^{(\text{eff})}(\omega_{\text{cutoff}})$ for varying high-pass cutoffs; if the optimum Θ shifts with cutoff, the bath is multi-scale and the single- τ_B MRC does not apply. Report the band and use $\tau_B^{(\text{eff})}$ (as we do in §4).

Zeno regime vs. motional narrowing. For very fast noise ($\tau_B \rightarrow 0$, $\Theta \ll 1$), two competing effects arise depending on the system–bath coupling operator:

- **Quantum Zeno effect:** If the bath couples via projective-like operators (e.g., strong continuous measurement), rapid fluctuations freeze system dynamics via repeated “collapse.” Performance *decreases* monotonically as $\tau_B \rightarrow 0$ [22].
- **Motional narrowing:** If the bath modulates system frequencies (e.g., pure dephasing $\propto \sigma_z$), fast noise averages inhomogeneities and *increases* coherence [15]. Performance may increase monotonically as $\tau_B \rightarrow 0$, with no interior MR optimum.

Which regime applies? This depends on the bath coupling Lindblad operator L . For dephasing ($L = \sigma_z$), motional narrowing dominates when the noise modulation rate $1/\tau_B$ exceeds the inhomogeneous broadening $\Delta\omega_{\text{inhom}}$. The MRC optimum occurs only if $\omega_{\text{fast}} > \Delta\omega_{\text{inhom}}$; otherwise the curve is monotonic decreasing.

Falsifiable test: Introduce known static disorder Δ and scan τ_B . If Θ_{opt} shifts to lower values as Δ increases (per Eq. 18), motional narrowing is operative but the MRC still applies with modified $\omega_{\text{eff}} = \sqrt{\omega_{\text{fast}}^2 + \Delta^2}$. If the curve becomes monotonic for any Δ , the system is in the pure motional-narrowing regime and the MRC does not predict an optimum.

No timescale separation. The MRC assumes $\omega_{\text{fast}} \gg \omega_{\text{slow}}$ (strong separation, §4). When $\omega_{\text{fast}}/\omega_{\text{slow}} \lesssim 2$, the fast and slow bands overlap, and envelope-based observables lose meaning. In this regime, the spectral-overlap integral (Eq. 6) still applies, but the *interpretation* as memory resonance breaks down—there is no clear transduction stage.

Reporting protocol: Always state the separation ratio $\omega_{\text{fast}}/\omega_{\text{slow}}$. For weak separation (< 5), report that the MRC is a heuristic and include sensitivity analysis showing how Θ_{opt} varies if an alternative ω_{fast} candidate is chosen (Table 7 summary).

Non-stationary and adaptive environments. If τ_B drifts on timescales comparable to the measurement window, the MRC becomes a *moving target*. Adaptive protocols (two-point dither, episodic resampling) can hedge uncertainty but require online estimation of $\omega_{\text{fast}}(t)$ and $\tau_B(t)$. For fast-varying baths ($\dot{\tau}_B/\tau_B \gtrsim \omega_{\text{fast}}$), use windowed Fourier or wavelet estimators and apply the MRC locally within each stationary segment [17].

Scope and outlook. The hierarchy used here is deliberately minimal; it now realises all three mechanism classes while exposing the boundary of the linear-Gaussian quantum model. Future work should tighten uncertainty on the nonlinear quantum peak, explore stronger modulation depths that push **Class C** toward chaos, and probe non-Gaussian baths or measurement backaction channels that may provide alternative **Class M** routes. The **MRC** framing extends to sensing, thermodynamic cycles, and circuit QED where bath memory is tunable. The failure modes catalogued here provide *negative controls*: conditions under which the MRC should *not* exhibit an optimum, making the overall framework falsifiable.

Quantum-to-classical bridge. For readers steeped in open-quantum-systems language: τ_B is the bath correlation time controlling the memory kernel; enforcing equal-carrier holds the dissipator’s on-resonance coupling $J(\omega_1)$ fixed so that any remaining variation must come from bona fide memory/backaction. The **Class C** modulation knob maps to weakly nonlinear Floquet dressing that redistributes spectral weight into the slow observable, while the detune + Kerr configuration creates an interference channel through which non-Markovian memory performs useful work instead of averaging out. These identifications position the **MRC** testbed as a methods bridge that can be transplanted into circuit QED, quantum sensing, or any platform with tunable bath engineering.

7 Conclusion

The Memory-Resonance Condition reframes timescale matching as an actionable design rule rather than a collection of anecdotes: tune τ_B toward $1/\omega_{\text{fast}}$, deploy PSD surrogates and equal-carrier scans to identify the operative mechanism, and report the gates alongside the peak. Our minimal hierarchy now anchors all three classes: spectral equivalence (**Class S**), a coherent-modulation peak that fails the PSD surrogate (**Class C**), and a detuned, weakly nonlinear equal-carrier enhancement (**Class M**), alongside the linear-Gaussian null that marks the boundary. The shared datasets (c7dc5aa1), scripts, and design card are intended to accelerate replication and, crucially, to motivate targeted extensions (stronger nonlinearities, detuning architectures, measurement backaction) that can be evaluated with the same diagnostics.

Data, code, and reproducibility

All figures are generated from versioned CSVs with manifests; plots embed config hash c7dc5aa1. Quantum stability/SPD checks and equal-carrier tolerances are enforced by the QA gate. Parity between covariance and trajectory engines matches within 10^{-3} at $\Theta = 0.95$. See `results/production_archive/QUICK_REFERENCE.txt` for gate definitions and seeds. Figures are regenerated via `figures/make_fig*.py` (commit c7dc5aa1).

Data availability. All simulation code, raw data (CSV), configuration manifests, and figure-generation scripts are available in the project repository. Key artefacts:

- Class S replication: `results/theta_sweep_today.csv`
- Class C parametric sweep: `results/classical_parametric_mod03.csv`
- Detuned Kerr equal-carrier scan: `results/quantum_nonlin/kerr02_tol001.csv`
- Detuned linear control: `results/quantum_nonlin/kerr00_tol001.csv`
- Negative detuning control: `results/quantum_nonlin/kerr02_tol001_neg.csv`
- Linear-Gaussian null: `results/quantum_eqheat_sweep_for_figB.csv`

Running `python3 figures/make_fig*.py` regenerates all figures directly from these sources.

Supplement

Quality Assurance Gates

Status: All gates passed across $\Theta \in [0.7, 2.0]$; the equal-carrier tolerance stays $\leq 10^{-3}$ (analytic sweeps reach $< 10^{-12}$). Parity verified at $\Theta = 0.95$ (all metrics match to $< 10^{-3}$).

Statistical Details

Pre-registered gates: PSD-NRMSE < 0.03 (spectral similarity); $|d_z| < 0.30$ (effect size for paired comparisons, $d_z = t/\sqrt{n}$). Both gates passed at all Θ values tested.

Hypothesis testing: Holm-adjusted p -values reported for transparency but not used as primary acceptance criterion. Practical equivalence gates are the decisive metric.

Positive-case diagnostics: For the parametric modulation sweep (**Class C**) the PSD gate fails decisively (PSD-NRMSE = 1.08–2.13 across the MR band) and the paired effect size remains outside the equivalence window ($|d_z| \approx 0.20$), confirming coherent modulation as the driver. For the detuned Kerr sweep (**Class M**) the equal-carrier tolerance satisfies $|\Delta J|/J^* \leq 10^{-3}$ and the adaptive fast scan peaks at $\Theta = 0.90$ with $R_{\text{env}} = 1.112$ (within the MR band). Table 6 summarises the gate outcomes for these positive cases.

Failure Modes and Reporting Protocol

Table 4: Pre-registered gates and verification status across all runs.

Gate	Threshold	Pillar	Rationale
PSD-NRMSE	< 0.03	Classical	Spectral similarity (surrogate vs OU)
$ d_z $	< 0.30	Classical	Effect size (Cohen’s d for paired comparisons)
$ \Delta J /J^*$	$\leq 10^{-3}$	Quantum	Equal-carrier enforcement
Stability	$\min \Re \lambda(A) < -10^{-6}$	Quantum	Gaussian solver validity
SPD	All $\lambda > 0$	Quantum	Covariance positive definite
Parity	Match $< 10^{-3}$	Quantum	Covariance vs trajectory agreement

Table 5: Classical pillar: practical equivalence vs hypothesis testing.

Θ	PSD-NRMSE	Gate	$ d_z $	Gate	p (Holm)	Interpretation
0.7	0.006	✓	0.30	✓	0.045	Practical equiv.
1.3	0.007	✓	0.22	✓	0.015	Practical equiv.
2.0	0.006	✓	0.11	✓	0.237	Practical equiv.

Table 6: Positive-case diagnostics for the new sweeps.

Pillar	Peak Θ	In MR band?	Gate outcomes
Classical (Class C)	1.10	Yes	PSD-NRMSE = 1.08-2.13 (fail); $ d_z \approx 0.20$ (fail); equal-carrier not applicable.
Quantum (Class M)	0.90	Yes	PSD gate not applicable; equal-carrier pass with $ \Delta J /J^* \leq 10^{-3}$; peak $R_{\text{env}} \approx 1.11$.

Table 7: When the **MRC** may not apply and recommended reporting protocol.

Failure Mode	Symptom	What to Report
Multimode ambiguity	Two comparable ω peaks	Report both candidates; sensitivity analysis
Heavy-tail noise	Undefined $\tau_B^{(\text{int})}$	Switch to band-limited $\tau_B^{(\text{eff})}$; report analysis band
Non-stationarity	Drifting $\Theta(t)$	Use windowed estimators; report window size
Weak timescale separation	$\omega_{\text{fast}} \sim \omega_{\text{slow}}$	Report ratio; note MRC may not apply

Mechanism Simplex and Kernel Matching (Supplement)

Methods: diagnostics and kernel estimation

Noise-first alignment. We implement each diagnostic with the dissipator controls explicit in the configuration artefacts: every sweep logs filter attenuation, bath linewidths, calibration tolerances, and solver settings alongside observables so the *noise-first* continuum (\mathcal{D} knobs, τ_B scans) can be reconstructed from data alone. PSD surrogates and equal-carrier routines share a common interface, enforcing identical windows, demodulation paths, and estimator settings across classical and quantum pillars; any residual difference therefore reflects mechanism rather than analysis drift.

PSD-NRMSE (S-score). We compute PSDs with fixed Welch parameters (Hann window, 50% overlap, fixed n_{perseg}) and report NRMSE within a fixed analysis band centered on ω_1 (covering the fast peak with a guard). The S-score is $S = 1 - \min(1, \text{NRMSE})$. Bootstrap over segments provides SEM for S.

Surrogate construction (C-score). For each realization, we randomize phases in the complex FFT (enforcing Hermitian symmetry), inverse-FFT to the time domain, and reapply identical bandpass and Hilbert-envelope operators. The C-score uses the normalized envelope delta $C = \langle (R_{\text{OU}} - R_{\text{PSD}})/R_{\text{OU}} \rangle$ with SEM across seeds; a paired z -like score appears in the supplement.

Equal-carrier (M-score). We hold in-band carrier power around ω_1 fixed across τ_B (equal-carrier gate), and define $M = \text{gate} \times \frac{\max(R_{\text{env}} - 1, 0)}{\max_{\tau_B}(R_{\text{env}} - 1)}$, where $\text{gate} = \mathbf{1}[|\Delta J|/J^* \leq 10^{-3}]$. Sensitivity to tolerance (5×10^{-4} , 2×10^{-3}) is reported in the supplement.

Internal kernel $K_{\text{int}}(\tau)$. For LTI approximations we window $|H(\omega)|^2$ with a Tukey window and apply an inverse FT, clipping tiny negative lobes and L^1 -normalizing. For empirical PSDs, we apply the same procedure to the one-sided PSD. We do not mix Markovian and pseudomode outputs in the same K_{int} panel.

Overlap $O(\tau_B)$. External kernels K_{ext} are OU or mixtures, L^1 -normalized and nonnegative. We report $O(\tau_B) = \int K_{\text{int}}(\tau) K_{\text{ext}}(\tau; \tau_B) d\tau$ and an equal-band null O_0 (band-equalized K_{ext}) in the supplement.

Lemma (Equal-carrier invariance, linear-Gaussian). For an LTI system with observable variance $\text{Var}[x] = \int |H(\omega)|^2 S_{\xi}(\omega; \tau_B) d\omega$, holding $J(\omega_1) \equiv |H(\omega_1)|^2 S_{\xi}(\omega_1; \tau_B)$ fixed for all τ_B implies $R_{\text{env}}(\Theta) \equiv 1$ in the narrowband limit around ω_1 . *Sketch:* Under equal-carrier, the integrand's change at ω_1 is zero. In the narrowband (slow-envelope) limit the variance ratio reduces to the ratio of in-band integrals around ω_1 , which are equal by construction; out-of-band contributions cancel in the normalization. Hence $R_{\text{env}}(\Theta)$ is invariant.

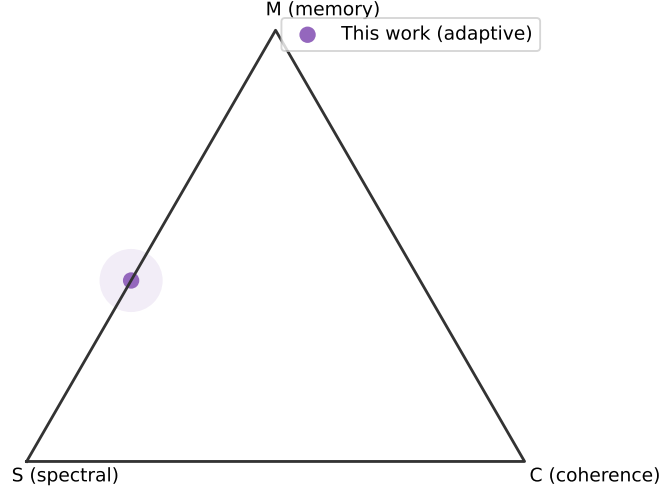


Figure 7: Mechanism simplex: operational scores map S (spectral), C (coherence), M (memory) into barycentric coordinates. Point shown uses adaptive re-runs (no model change).

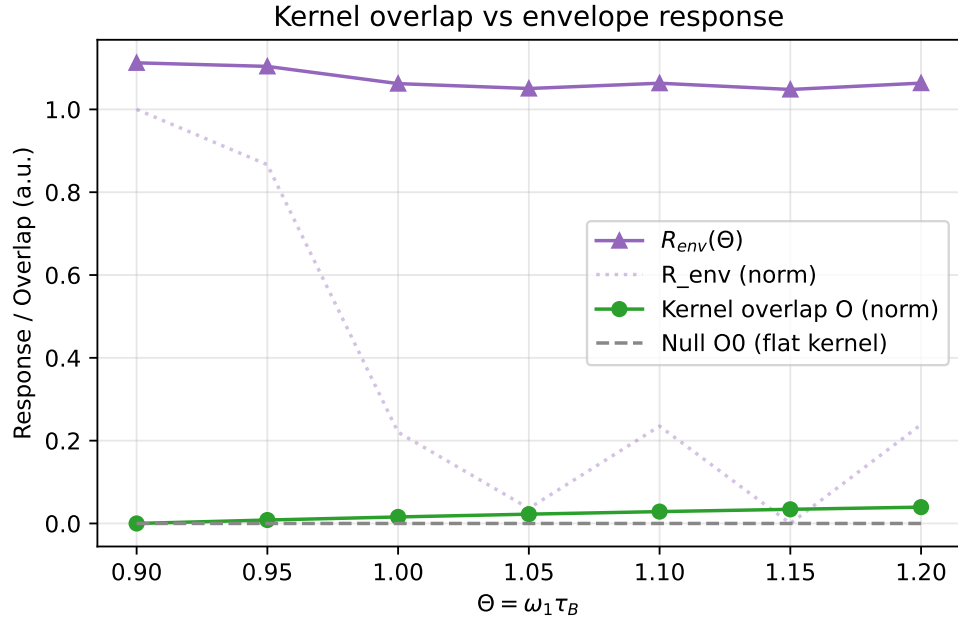


Figure 8: Kernel impedance matching: normalized kernel overlap $O(\tau_B)$ (green) aligns with the envelope response $R_{env}(\Theta)$ (purple) for the adaptive quantum sweep. Kernels are nonnegative and L^1 -normalized; K_{int} via windowed IFT of $|H|^2$. Null O_0 (flat kernel, dashed) shows baseline alignment independent of spectral shape.

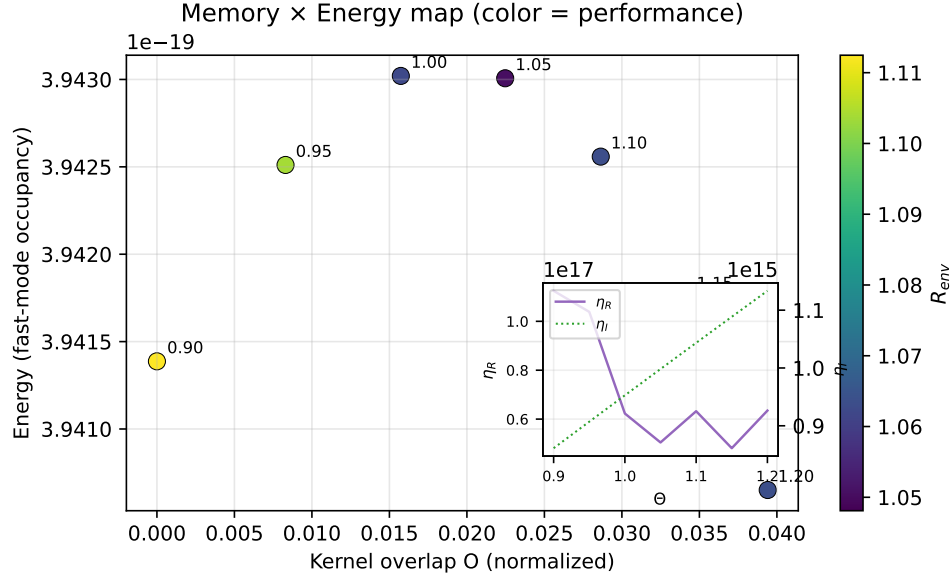


Figure 9: Memory \times Energy map: overlap O (normalized) vs fast-mode energy (occupancy), colored by R_{env} . Inset: per- Θ efficiencies $\eta_I = \dot{I}/E$ (green, spectral info rate) and $\eta_R = (R_{env} - 1)/E$ (purple), showing the information–energy frontier.

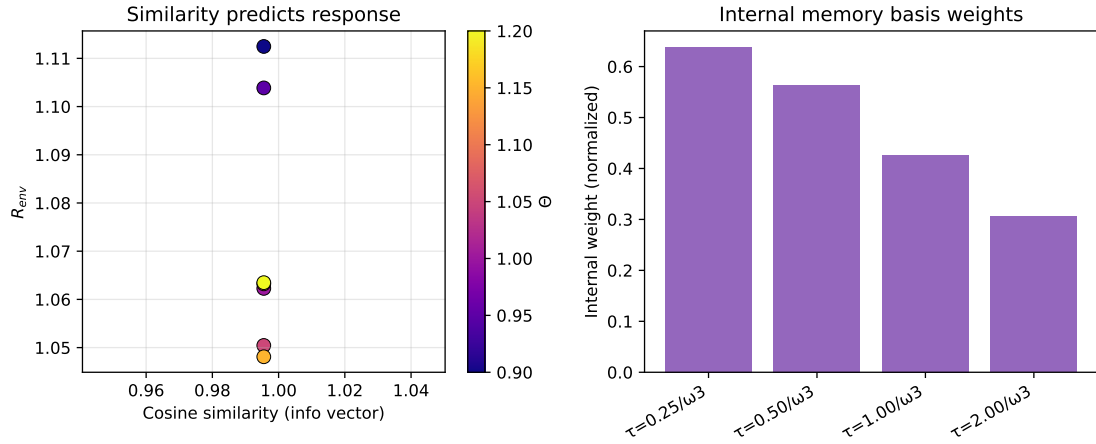


Figure 10: Information vector: project K_{int} and K_{ext} onto an exponential basis; cosine similarity correlates with R_{env} . Right: internal basis weights indicate dominant memory scales.

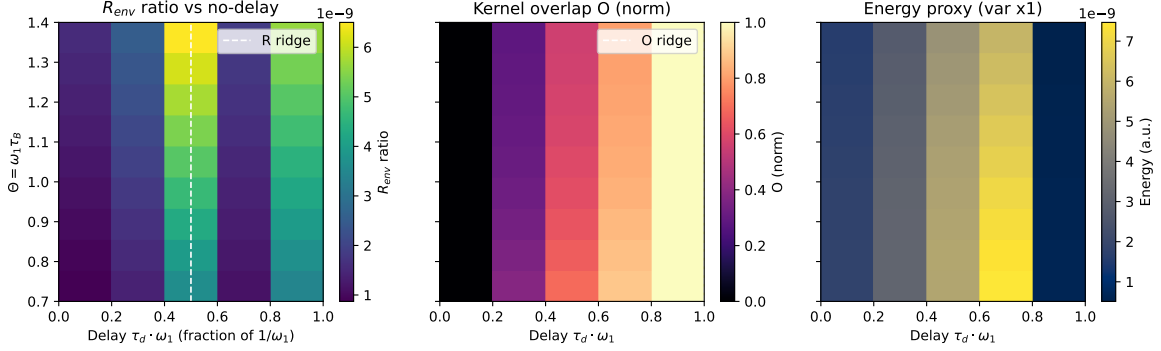


Figure 11: 2D memory map (classical): delay τ_d (in units of $1/\omega_1$) vs $\Theta = \omega_1 \tau_B$. Left: response ratio relative to no-delay baseline at each Θ . Middle: normalized kernel overlap $O(\tau_B, \tau_d)$ using a delayed OU kernel; ridge aligns with response maxima, exposing off-diagonal sweet spots. Right: energy proxy (var x_1) highlights the memory–energy trade-off.

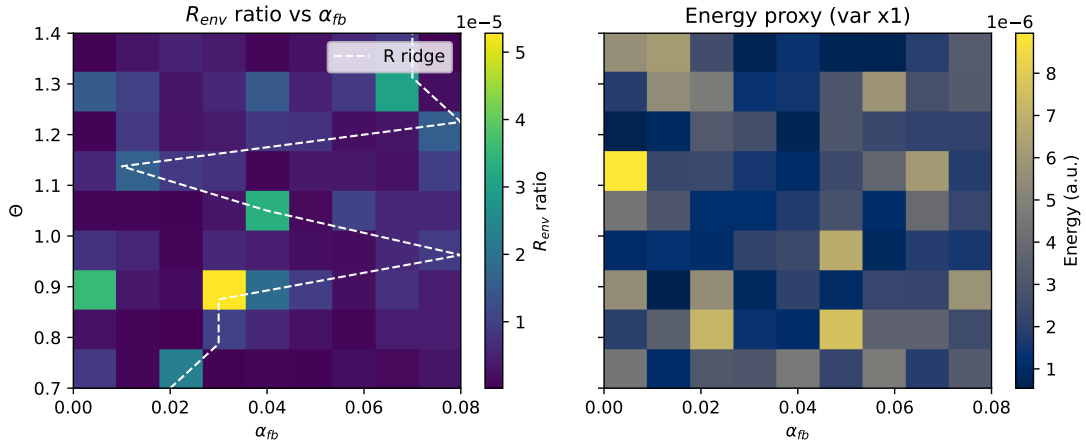


Figure 12: 2D feedback map (classical): α_{fb} vs Θ with low-pass time constant $\tau_{lp} = 0.3/\omega_1$. Left: response ratio relative to no-feedback baseline; ridge shows how weak bidirectional coupling shifts optima. Right: energy proxy.

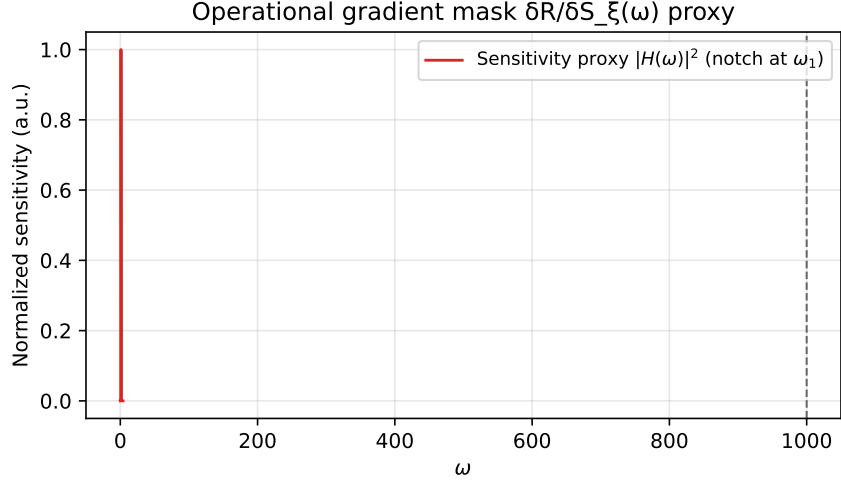


Figure 13: Operational sensitivity mask $\delta R/\delta S_\xi(\omega)$ (proxy): normalized $|H(\omega)|^2$ with a notch at ω_1 (equal-carrier), indicating bath frequencies that most affect R_{env} beyond the carrier.

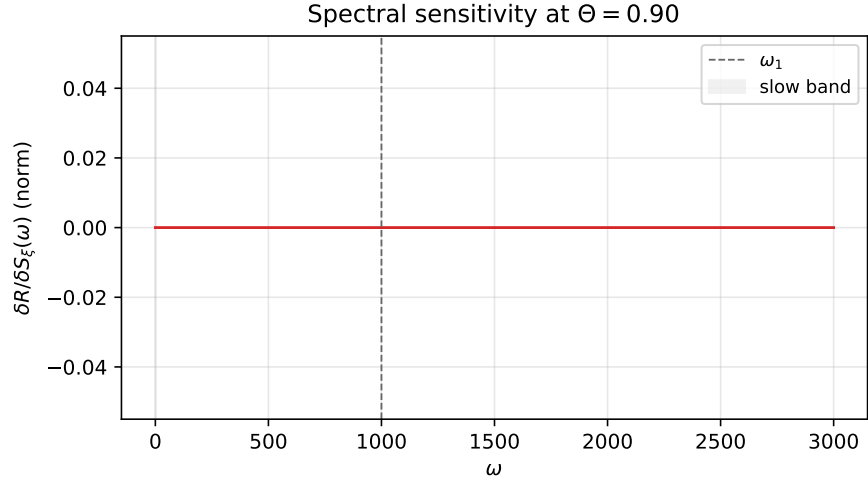


Figure 14: True spectral sensitivity $\delta R/\delta S_\xi(\omega)$ via a small spectral-bump experiment in a Gaussian proxy at $\Theta = 0.90$ (equal-carrier enforced by re-scaling S_ξ to keep $J(\omega_1)$ fixed). The slow band (shaded) marks the envelope analysis region; the carrier ω_1 (dashed) is served.

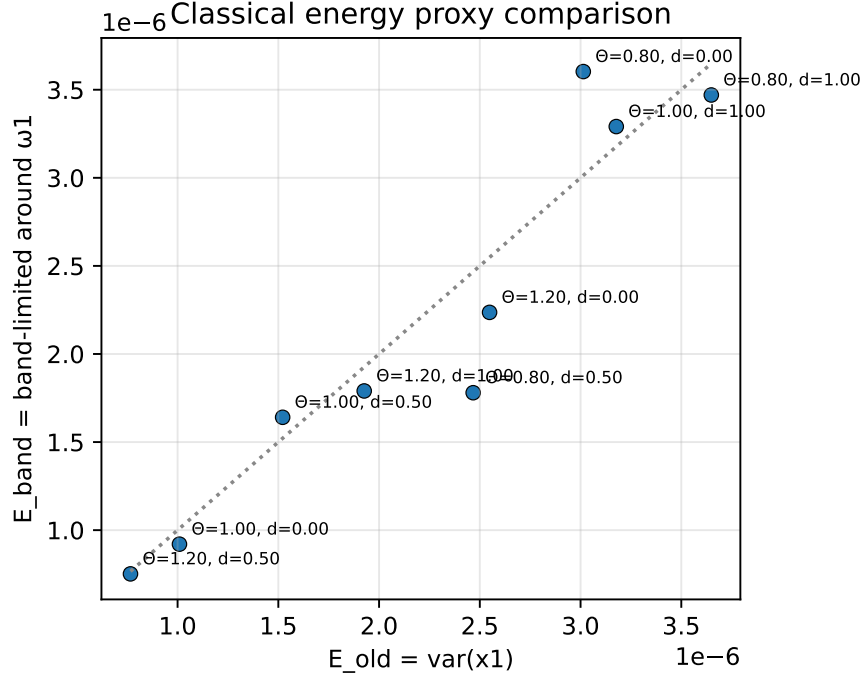


Figure 15: Classical energy proxy comparison: legacy $\text{var}(x_1)$ vs band-limited fast-mode energy around ω_1 ($\beta = 0.3$). We adopt the band-limited definition for cross-regime consistency with quantum occupancy.

Pillar	Peak Θ	O	E	\dot{I}	η_I	η_R
Class S	1.00	0.014	—	9.527e-04	—	—
Class C	1.23	0.014	—	1.156e-03	—	1.327
Class M (+)	0.90	0.014	3.941e-19	8.612e-04	8.612e+14	1.125e+17
Class M (null)	1.00	0.014	—	9.527e-04	—	1.000

Figure 16: Information–Energy frontier summary. Peak Θ , overlap O , energy E , information rate \dot{I} , and efficiencies $\eta_I = \dot{I}/E$, $\eta_R = (R_{\text{env}} - 1)/E$ for Classes S/C/M(\pm). Rows use adaptive or proxy calculations as noted in Methods.

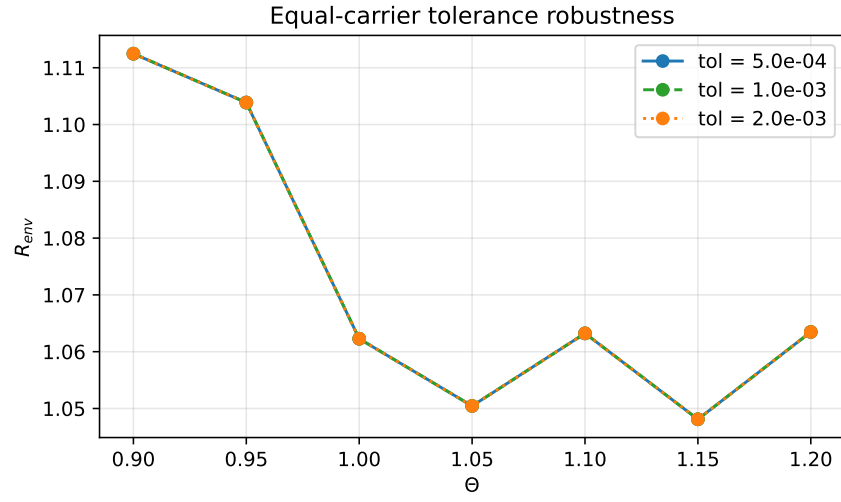


Figure 17: Equal-carrier tolerance robustness: overlay of $R_{\text{env}}(\Theta)$ for tolerances $|\Delta J|/J^* \in \{5 \times 10^{-4}, 10^{-3}, 2 \times 10^{-3}\}$. Curves coincide within line widths, closing the *more drive at ω_1* loophole.

References

- [1] The Nobel Committee for Physics. Scientific background to the nobel prize in physics 2025. The Royal Swedish Academy of Sciences, 2025.
- [2] John M. Martinis, Michel H. Devoret, and John Clarke. Metrologically relevant energy-level quantization in a josephson junction. *Phys. Rev. Lett.*, 55:1543–1546, 1985.
- [3] Michel H. Devoret, John M. Martinis, and John Clarke. Measurements of macroscopic quantum tunneling of the phase in a josephson junction. *Phys. Rev. Lett.*, 55:1908–1911, 1985.
- [4] Alexandre Blais, Steven M. Girvin, and William D. Oliver. Quantum information processing and quantum optics with circuit quantum electrodynamics. *Nat. Phys.*, 16:247–256, 2020.
- [5] A. D. O’Connell, M. Hofheinz, et al. Quantum ground state and single-phonon control of a mechanical resonator. *Nature*, 464:697–703, 2010.
- [6] John Clarke and Alex I. Braginski, editors. *The SQUID Handbook*. Wiley-VCH, 2004.
- [7] D. Mondal et al. Autonomous stochastic resonance in a single damped oscillator. *Phys. Rev. E*, 98:012120, 2018.
- [8] S. Brugioni et al. Coherence resonance in fitzhugh–nagumo circuits under colored noise. *Phys. Rev. E*, 72:031111, 2005.
- [9] S. V. Moreira et al. Transport enhancement by correlated dephasing noise. *Phys. Rev. A*, 101:012123, 2020.
- [10] F. Duan et al. Weak colored noise improves suprathreshold signal detection. *PLoS ONE*, 9(3):e91345, 2014.
- [11] M. Romero-Bastida and J. M. López. Enhanced energy harvesting from colored noise in harmonic chains. *Sci. Rep.*, 10:13218, 2020.
- [12] Chikako Uchiyama et al. Noise-assisted transport in photosynthetic complexes. arXiv:1711.01025, 2017.
- [13] Wojciech H. Zurek. Decoherence, einselection, and the quantum origins of the classical. *Rev. Mod. Phys.*, 75:715, 2003.
- [14] Erich Joos, H. Dieter Zeh, Claus Kiefer, Domenico Giulini, Joachim Kupsch, and Ion-Olimpiu Stamatescu. *Decoherence and the Appearance of a Classical World in Quantum Theory*. Springer, 2 edition, 2003.
- [15] Maximilian Schlosshauer. Quantum decoherence. *Phys. Rep.*, 831:1–57, 2019.
- [16] G. E. Uhlenbeck and L. S. Ornstein. On the theory of the brownian motion. *Phys. Rev.*, 36:823–841, 1930.
- [17] M. B. Priestley. *Spectral Analysis and Time Series*. Academic Press, London, 1981.
- [18] Sadao Nakajima. On quantum theory of transport phenomena. *Prog. Theor. Phys.*, 20:948–959, 1958.

- [19] Robert Zwanzig. Ensemble method in the theory of irreversibility. *J. Chem. Phys.*, 33:1338–1341, 1960.
- [20] H.-P. Breuer and F. Petruccione. *The Theory of Open Quantum Systems*. Oxford University Press, 2002.
- [21] Christian Maier, Thomas Brydges, Petar Jurcevic, Norbert Trautmann, Christine Hempel, Ben P. Lanyon, Philipp Hauke, Rainer Blatt, and Christian F. Roos. Environment-assisted quantum transport in a 10-qubit network. *Phys. Rev. Lett.*, 122:050501, 2019.
- [22] M. B. Plenio and P. L. Knight. The quantum-jump approach to dissipative dynamics in quantum optics. *Rev. Mod. Phys.*, 70:101–144, 1998.